MULTIMODAL IMAGING ASSESSMENT OF POST-TRAUMATIC OSTEOARTHRITIS PROGRESSION

by

AMANVEER SINGH

A dissertation submitted in partial fulfillment of the
requirements for the degree of

DOCTOR OF PHILOSOPHY IN BIOMEDICAL SCIENCES:

MEDICAL PHYSICS

2025

Oakland University
Rochester, Michigan

Doctoral Advisory Committee:

Yang Xia, Ph.D., Chair
Bradley J Roth, Ph.D.
Eugene Surdutovich, Ph.D.
Quan Jiang, Ph.D.
Steffan Puwal, Ph.D.

Thank you to the Universe for the experience of life.
Thank you to all my Friends and Family.
Thank you to my dear parents, my father Harmohinder Singh, my mother Narinder Kaur, and my sister Gunjan Singh, for their unwavering love and support throughout my life.
Thank you to my two most special friends, my wife Jasleen Kaur and my cat Mr. Jack Pumpkin for their invaluable companionship and love.
Blessed to have you all!!

ACKNOWLEDGMENTS

This research was conducted in the Department of Physics (Medical Physics Program), Oakland University, Rochester, MI. I am highly grateful to my adviser, Yang Xia, Ph.D., for the opportunity to work in his lab and for his unwavering encouragement and guidance throughout my research journey. His mentorship has been invaluable in my scientific and personal growth. I extend my sincere gratitude and respect to Bradley Roth, Ph.D., for the opportunity to join the Medical Physics program and for his constant support. I am very thankful to Eugene Surdutovich, Ph.D., for his expertise and guidance throughout my research at Oakland University. I also want to sincerely thank Quan Jiang, Ph.D., and Steffan Puwal, Ph.D., for their invaluable support and for being part of the dissertation committee. I had the opportunity to work with great researchers in our lab. I am especially thankful to Farid Badar, Ph.D., for help with imaging procedures. I also want to acknowledge my fellow lab mates, Syeda Batool, Ph.D., Hannah Mantebea, Ph.D., Austin Tetmeyer, Aaron Blanc, and Sarah Salem, for their help and collaboration. I am thankful to the faculty and staff of the Physics Department at Oakland University for their support over the years. I appreciate Michael Newton, Ph.D., and Kevin Baker, Ph.D., at the Beaumont Research Institute for their assistance with surgical procedures during the study. I extend my heartfelt gratitude to all the rabbits that were ethically used in the research. I want to thank the assistantship support from the Center for Biomedical Research at Oakland University. I greatly appreciate the financial support from the National Institutes of Health (AR069047) which made this research possible.

Amanveer Singh

ABSTRACT

MULTIMODAL IMAGING ASSESSMENT OF POST-TRAUMATIC OSTEOARTHRITIS PROGRESSION

by

AMANVEER SINGH

Adviser: Yang Xia, Ph.D.

Osteoarthritis (OA) is a complex joint disease that can cause progressive damage that leads to chronic pain, stiffness, and functional impairment, which can severely affect the quality of a person's life. The primary reason for the development of OA is the degeneration of articular cartilage which acts as a smooth load-bearing surface in diarthrodial joints. Post-traumatic osteoarthritis (PTOA) is a specific form of OA that occurs after joint injury. The architecture and operation of articular cartilage are special and depend on its dense extracellular matrix (ECM); PTOA results in significant ECM changes which lead to cartilage degradation and structural failure. Due to the avascular nature of cartilage, its self-repair capacity remains limited, thus its degradation will benefit from early detection and intervention. The study of PTOA progression is critically dependent on advanced imaging methods. For example, magnetic resonance imaging (MRI) is a sensitive tool for detailed assessment of cartilage health and can assist in the early detection of disease; polarized light microscopy (PLM) is effective for the detailed assessment of collagen fiber orientation and structural integrity of the cartilage; and computed tomography (CT) imaging can measure subchondral bone remodeling. These

imaging techniques probe different aspects of cartilage degradation; when used in combination, they can help to better understand OA progression which can lead to early diagnosis and more effective intervention.

This dissertation consists of eight chapters that investigate PTOA progression through high-resolution imaging. The first three chapters introduce this dissertation research by explaining knee joint OA while reviewing literature about its pathophysiology and advanced imaging capabilities for detecting early disease changes. The experimental design and imaging approaches for studying topographical and depth-dependent cartilage changes are explained in Chapter Four. The dissertation presents three peer-reviewed journal articles in chapters five through seven, offering new insights into cartilage degeneration in OA. Chapter Five explores the progression of PTOA and biomechanical factors involved in PTOA progression using μMRI imaging of the whole knee joint. Chapter Six investigates zonal structural changes in articular cartilage following a mechanical injury utilizing high-resolution μMRI imaging of cartilage blocks. Chapter seven examines the effects of an impact injury on articular cartilage and subchondral bone through PLM and μCT imaging. The final chapter summarizes results of this dissertation study and discusses potential future research directions.

TABLE OF CONTENTS

TABLE OF CONTENTS—Continued

TABLE OF CONTENTS—Continued

TABLE OF CONTENTS—Continued

LIST OF FIGURES

LIST OF TABLES

LIST OF ABBREVIATIONS

OA	Osteoarthritis
PTOA	Post-traumatic osteoarthritis
ECM	Extracellular matrix
MRI	Magnetic resonance imaging
PLM	Polarized light microscopy
CT	Computed tomography
SZ	Superficial zone
TZ	Transitional zone
RZ	Radial zone
μMRI	Microscopic magnetic resonance imaging
μCT	Microscopic computed tomography
ACL	Anterior cruciate ligament
PCL	Posterior cruciate ligament
MCL	Medial collateral ligament
LCL	Lateral collateral ligament
W.W.	Wet weight
GAG	Glycosaminoglycan
MMPs	Metalloproteinases
NMR	Nuclear magnetic resonance
SNR	Signal-to-noise ratio
SE	Spin echo

TE	Echo time
FOV	Field of view
TR	Repetition time
HU	Hounsfield unit
BMD	Bone mineral density
ICP	Inductively coupled plasma
OES	Optical emission spectroscopy
RF	Radio frequency
SSG	Slice selection gradient
PEG	Phase encoding gradient
FEG	Frequency encoding gradient
PI	Protease inhibitors
ROI	Regions of interest
NIK	Non-impact knee
IK	Impact knee
CZ	Calcified zone
SBP	Subchondral bone plate
AC	Articular cartilage
STB	Subchondral trabecular bone

LIST OF PUBLICATIONS

This dissertation is based on the following original research articles:

I. Singh A, Mantebea H, Badar F, Batool S, Abdelmessih G, Sebastian T, Newton M, Baker K, Salem S, Xia Y. Assessment of articular cartilage degradation in response to an impact injury using μMRI. Connect Tissue Res. 2024 Mar;65(2):146-160. doi: 10.1080/03008207.2024.2319050.

II. Singh A, Mantebea H, Badar F, Batool S, Tetmeyer A, Abdelmessih G, Sebastian T, Newton M, Baker K, Salem S, Xia Y. Assessment of post-trauma microstructural alterations in the rabbit knee cartilage and subchondral bone. J Anat. 2024 Nov;245(5):740-750. doi: 10.1111/joa.14102.

III. Singh A, Tetmeyer A, Chong P, & Xia Y. Progression of Post-Traumatic Osteoarthritis Over 14 Weeks Following a Subcritical Injury. Submitted to Magnetic Resonance Imaging (2025).

The copyright holders have granted permission to reproduce the original research articles.

CO-AUTHORED ARTICLES

I. Mantebea H, Batool S, Singh A, Hammami M, Badar F, Xia Y. Structural differences between immature and mature articular cartilage of rabbits by microscopic MRI and polarized light microscopy. J Anat. 2022 Jun;240(6):1141-1151. doi: 10.1111/joa.13620.

II. Mantebea H, Singh A, Badar F, Abdelmessih G, Sebastian TM, Baker K, Newton M, Xia Y. Characteristics of distal femoral articular cartilage in 6 weeks posttraumatic osteoarthritis by a subcritical impact. J Orthop Res. 2024 Apr;42(4):717-728. doi: 10.1002/jor.25721.

CHAPTER ONE

INTRODUCTION

Post-traumatic osteoarthritis (PTOA) represents a specific form of osteoarthritis (OA) that develops after a joint injury occurs. The onset of PTOA can begin from injuries such as direct joint trauma, cartilage or meniscal damage, or ligament tears. While primary OA develops slowly over the years due to age-related factors, PTOA can develop much more quickly after an injury leading to joint pain and stiffness [1]. PTOA is significant from clinical and socioeconomic viewpoints because it can result in long-term disability and permanent joint damage in the younger population that may require total knee replacement. The disease management of PTOA is difficult because of its complex and silent progression. The joint experiences cartilage degradation with inflammation and subchondral bone changes due to mechanical and metabolic alterations following an injury [2]. After an injury, chondrocytes, the cells present in the cartilage produce inflammatory cytokines and matrix-degrading enzymes that speed up tissue breakdown. The injury disrupts the synovial environment which leads to further progression of PTOA [3]. The inability of cartilage to heal naturally requires prompt detection and intervention to prevent permanent joint degradation.

Covering the ends of bones, articular cartilage is a form of connective tissue that is specific to joints and is required for joint movement and function. The smooth surface of articular cartilage acts as a shock absorber and functions to decrease friction so that joints can move easily [4-6]. The main composition of articular cartilage consists of a small population of chondrocytes and an extracellular matrix (ECM) made up of water,

collagen fibers, and proteoglycans [7]. The morphological structure of the cartilage is divided into three sub-tissue zones. The first zone is called the superficial zone (SZ), which has collagen fibers arranged parallel to the surface. Beneath it is the transitional zone (TZ) that has randomly oriented collagen fibers. The third zone, called the radial zone (RZ), has collagen fibers that are oriented perpendicular to the surface [8, 9]. Since cartilage cannot heal itself, following an injury the tissue breaks down progressively leading to the worsening of PTOA [10]. Given the vital role cartilage plays in joint functioning, detecting early degradation in cartilage becomes crucial for stopping OA from getting worse. Conventional diagnostic tools such as X-rays can only determine changes in the bone but cannot show cartilage degradation in the early stage [11, 12], while magnetic resonance imaging (MRI) is sensitive to water molecules in the tissue, which makes it a powerful technique to assess the integrity of articular cartilage and to identify early degenerative changes [12-14]. High-resolution tissue imaging helps in the observation of specific structural alterations in complex joints which lead to PTOA development. MRI helps diagnose OA by assessing cartilage condition while the computed tomography (CT) imaging monitors subchondral bone changes. In addition, polarized light microscopy (PLM) is an essential imaging tool for studying cartilage's collagen structure in detail. The combination of these tools has significant potential to enhance the monitoring of OA development which could lead to better treatment options.

This dissertation investigates PTOA development in a rabbit model following a subcritical impact injury to the femoral articular cartilage, presented through three phases of the project. The specific objectives for each phase:

1. Using MRI T2 mapping as a tool to track femoral cartilage degradation from 0 to 14 weeks after a mechanical injury while examining how injury duration and force magnitude affect cartilage damage and PTOA development.

2. Using high-resolution microscopic magnetic resonance imaging (μMRI) to observe zonal transformations in articular cartilage after a knee injury by studying the structural alterations in the superficial zone, transitional zone, and radial zone.

3. Using high-resolution polarized light microscopy (PLM) and microscopic computed tomography (μCT) imaging to analyze early-stage cartilage and subchondral bone deterioration after a mechanical injury, aiming to develop better diagnostic methods for OA.

.

CHAPTER TWO

HEALTH AND DISEASE OF KNEE JOINT: THE IMPACT OF CARTILAGE DEGENERATION IN OSTEOARTHRITIS

2.1 Biomechanics of the Knee Joint

The knee joint, a marvel of biomechanical engineering is one of the largest and most complex joints in the human body that is made up of tibiofemoral and patellofemoral joints [15]. It is a synovial hinge joint which allows the body to flex and extend [16]. The anatomy of the knee joint (Figure 2.1) consists of four bones: femur, tibia, patella, and fibula. The femur at the tibiofemoral joint joins with the tibia to support most of the body's weight. The patellofemoral joint has the patella which attaches to the femur to enable the quadriceps muscle to work effectively during the extension of the knee. The fibula is connected to the tibia and does not directly participate in the movement of the knee joint, but it does serve as a point of attachment for muscles, tendons, and ligaments [15, 16].

The soft tissues in the knee joint are essential for weight-bearing movement without pain or restriction [17]. Some of the key soft tissues include the menisci which act as a cushion between the tibia and femur, thus helping in the distribution of mechanical forces and protecting the articular cartilage [18]. Ligaments are bands of fibrous tissue that attach bones to other bones; major ligaments of the knee include the anterior cruciate ligament (ACL), posterior cruciate ligament (PCL), medial collateral ligament (MCL), and lateral collateral ligament (LCL), all of which help to stabilize the knee joint during movements [19]. Tendons are fibrous structures that attach muscles to

bones thus enabling joint movement and stabilization of the knee during different activities [20]. Articular cartilage is the tissue found at the end of the femur, tibia, and patella; it plays a crucial role in reducing friction between the bones during joint motion. The knee joint capsule also plays an important role in the stability of the joint by restricting excessive range of motion and preventing dislocation [21]. Bursae are fluid-filled sacs that lie between the tendons, muscles, and bones, their function is to decrease friction and pressure to allow easy and painless movements [22]. Synovial fluid, secreted by the synovial membrane lubricates the joint, nourishes the cartilage, and lowers friction, therefore preventing the wear and tear of the joint surfaces [23]. The soft tissues in the knee joint are functionally interlinked to ensure proper biomechanics and functioning.

2.2 Articular Cartilage

Cartilage is a form of connective tissue that is found in different parts of the body and offers support and flexibility to the body structure. There are three types of cartilage in the body: hyaline, fibrocartilage, and elastic. Articular cartilage (Figure 2.2) is a subtype of the hyaline cartilage that is present in diarthrodial joints and involved in supporting the skeletal system of the body [4]. The goal of this type of cartilage is to ensure that there is low-friction movement between the bones. In weight-bearing joints like the knee, articular cartilage is vital in the management of compressive stress and protection of the joint during movements [24]. The articular cartilage is composed of a dense extracellular matrix (ECM) and a small population of chondrocytes, the cells present in the articular cartilage that synthesize and maintain the ECM. ECM in the cartilage provides mechanical strength and elasticity to the tissue.

2.3 Composition of Articular Cartilage

On a compositional level, chondrocytes account for approximately 2% of the tissue by volume [6, 25]. The majority of the articular cartilage is its ECM, which is mainly composed of water (approximately 70-80% of the wet weight (w.w.)), collagen fibers (about 15% w.w.), and proteoglycans (5% w.w.). The concentration of water in the ECM varies across the tissue depth. It is the highest at the articular surface and progressively decreases towards the calcified region. Water is attached and retained by proteoglycans, helping to maintain the structure and resilience of the tissue. A smaller fraction of water is connected to collagen to form the collagen proteoglycan network [26]. Since cartilage is avascular, the high water content is important for nutritional and waste management [8].

Collagen is a protein found in connective tissues including cartilage, tendons, menisci, skin, and blood vessels. Although several types of collagens are found in the cartilage, type II collagen makes up approximately 80–90% of the total collagen content in articular cartilage [27]. Collagen in cartilage forms the three-dimensional fibrous network which gives the tissue its zonal architecture and is responsible for providing it with tensile strength. Healthy, non-calcified cartilage can be divided into three structural zones according to the collagen fiber orientation: densely packed collagen fibers in the superficial zone align parallel to the tissue surface which helps in resisting the shear forces. Randomly oriented collagen strands in the transitional zone and perpendicular collagen fibers in the radial zone help withstand compressive forces. Finally, there is also a calcified zone that anchors the non-calcified cartilage to the subchondral bone forming the contact plate between the cartilage and the underlying bone [27, 28].

Proteoglycans such as aggrecan, consist of a core protein that attaches to glycosaminoglycan (GAG) chains. GAGs are long, unbranched polysaccharides that are essential for the construction and function of cartilage [29]. The negatively charged sulphate groups on the GAG chains are responsible for attracting water. The charges on the GAG chains enable proteoglycans to bind water molecules to form a gel-like structure within the cartilage. Due to the water retention, the cartilage is able to resist compressive forces and retain its elasticity, which are both required for joint movement [30].

About two percent of the total volume in the adult human articular cartilage is made of cells called chondrocytes that are responsible for the maintenance of the cartilage throughout life [31]. The density of chondrocytes is highest in the upper tissues and decreases to one-third of the surface cell density in the deeper tissues. The structure of chondrocytes is determined by the arrangement of the surrounding collagen fibers. The cells are thin and flat in the superficial zone due to the tightly packed parallel collagen fibers. In the radial zone, the thicker collagen fibers that are perpendicular to the surface give the chondrocytes an ellipsoid shape. The response of chondrocytes to mechanical stress on the ECM can result in changes in cartilage synthesis [32, 33].

2.4 Articular Cartilage in Osteoarthritis

Osteoarthritis (OA) is a chronic joint disease that involves progressive degradation of articular cartilage. The enzymes in the ECM, matrix metalloproteinases (MMPs) and aggrecanases, are produced by chondrocytes in response to mechanical stress and inflammation which are responsible for the ECM degradation in OA [34]. When the proteoglycans and collagen are lost, the cartilage becomes weak and is unable to bear mechanical forces. The joint inflammation is worsened by the exposure of the

underlying bone as the cartilage deteriorates, leading to joint instability and discomfort [35]. The knee is one of the most affected joints by OA. Cartilage degradation can result in joint space narrowing, osteophyte formation, and subchondral bone sclerosis [36]. Knee OA that mainly affects the older population can severely impact their lives causing discomfort and stiffness, with limited motion of the joint.

2.5 Post-Traumatic Osteoarthritis

Post-traumatic osteoarthritis (PTOA) is a subtype of OA that develops after joint injury such as meniscal and ligament tears, direct cartilage damage, or bone fracture. PTOA can develop quickly following trauma compared to OA, which develops gradually over time. Injuries to the knee joint can often lead to PTOA with cartilage damage as one of the first symptoms of the disease [1]. PTOA progresses with both cartilage damage and indirect consequences like alterations in joint mechanics and inflammation. The damage to articular cartilage causes fibrillation and loss of proteoglycans therefore compromising the ability of the cartilage to support mechanical stress. These alterations lead to further deterioration, thinning, and finally the loss of cartilage over time. One of the critical features of PTOA is its rapid progression, the inflammatory response to the injury acts to accelerate the degradation by releasing cytokines that cause the breakdown of cartilage [2, 37]. PTOA can affect younger as well as older populations who are at risk of injuries causing long-term joint damage.

2.6 Animal Models for Studying Post-Traumatic Osteoarthritis

Animal models have been useful in providing important information about the pathogenesis and potential treatment of OA. Animal models like dog, rabbit, and rat are common among the animals used for OA studies. The rabbit model has been used

frequently due to its easy availability and similarities in biomechanical characteristics between rabbit and human cartilage. Among small animals, rabbits have adequate cartilage thickness for imaging and sufficient joint size for a controlled induction of surgical damage [38]. OA progression in animal models can be investigated using imaging technologies including MRI, CT, X-ray, and cartilage evaluation by histology. These techniques are useful in detecting changes in cartilage structure, bone remodeling, and joint space. The information on the molecular alterations in the cartilage can help in understanding the OA progression and the development of appropriate therapeutic interventions [39].

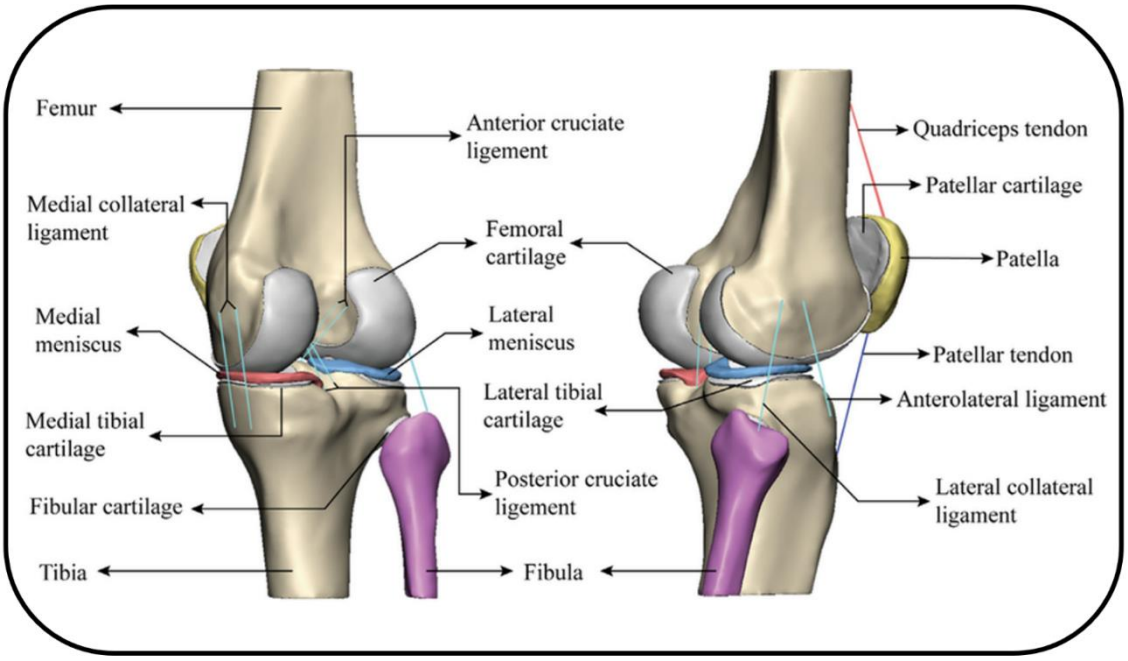

Figure 2.1 A three-dimensional representation of the knee joint anatomy showing the anatomical structures of the knee joint including bony and soft tissue components. Reprinted from [40], with permission.

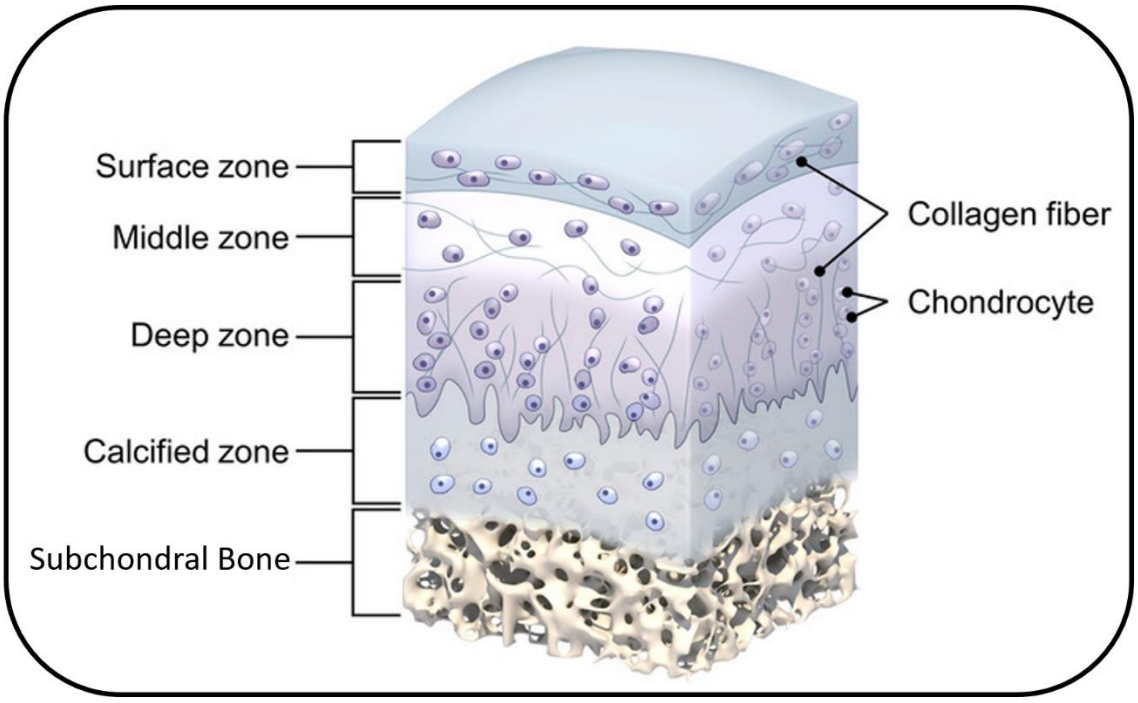

Figure 2.2 Schematic representation of articular cartilage structure showing the zonal organization, chondrocytes, collagen fibers orientation, and the subchondral bone interface. Reprinted from [41], with permission.

CHAPTER THREE

IMAGING MODALITIES FOR POST-TRAUMATIC OSTEOARTHRITIS

Although extensive research has been done on osteoarthritis (OA) and other joint diseases, there is still no effective treatment that can completely prevent or reverse cartilage loss. Hence there is an urgent need for better non-invasive imaging methods for diagnosis, prognosis, and management of the disease. The onset of this chronic disease is difficult to pinpoint, which is one of the biggest challenges in the diagnosis and management of OA. X-ray is one of the most commonly used and inexpensive techniques to diagnose OA through the assessment of joint space narrowing. However, the measurement of joint space in X-ray is not accurate, depending upon the orientation and position of the joint in the instrument. In addition, X-ray only shows evidence of OA when cartilage breakdown is apparent, hence it is not effective in evaluating cartilage composition and early biochemical alterations [42, 43]. Despite the limitations radiography is still the most accepted technique for OA diagnosis due to its easy accessibility and low cost. To achieve early and accurate detection of OA, more sensitive imaging methods like MRI are now being used in the management of OA in both the clinical and research fields.

3.1 Magnetic Resonance Imaging and Fundamentals of Nuclear Magnetic Resonance

Magnetic Resonance Imaging (MRI) is one of the most valuable and innovative tools for in-vivo assessment of cartilage and joint pathology, because of its high sensitivity to the motional environment of water molecules. MRI is a non-invasive technique that works on the principle of Nuclear Magnetic Resonance (NMR) to provide

cross-sectional images of the body with detailed information. Due to the ability to produce high-resolution images of soft tissues, MRI can provide detailed information on the composition of cartilage and its degenerative changes during OA progression [44].

MRI, based on the phenomenon of NMR, uses magnetic properties of atomic nuclei which are characterized by the nuclear spin angular momentum (S) and magnetic moment (μ). To understand the mechanism of MRI it is important to first understand the concept of nuclear spin. Spin angular momentum (S) is derived from the nuclear spin (I) which is a fundamental quantized property determined by the element's composition. For example, hydrogen nuclei (^{1}H) have a spin of ½, while deuterium (^{2}H) has a spin of 1. The magnitude of the spin angular momentum is given by the equation:

$$|\boldsymbol{S}| = (\boldsymbol{I}(\boldsymbol{I}+\boldsymbol{1}))^{\boldsymbol{1/2}}\ (\boldsymbol{h}/\boldsymbol{2\pi}) \qquad \textbf{3.1}$$

The z-component of the spin (Sz) is quantized and given by:

$$\mathbf{Sz} = \boldsymbol{m_I}(\boldsymbol{h}/\boldsymbol{2\pi}) \qquad \textbf{3.2}$$

where m_I is the magnetic quantum number which can take discrete values from -I to I and h is Planck's constant.

When a nucleus such as hydrogen is placed in an external magnetic field B_0, the spin of the hydrogen can align in one of two possible directions (parallel or anti-parallel) with respect to the magnetic field, resulting in two different energy levels. The lower energy state, where the spins align parallel to magnetic field B_0 is more populated and contributes more towards the net macroscopic magnetization in the sample. The population variation between the two energy levels is the key to the signal strength in magnetic resonance [45]. The net magnetization is along the direction of the applied magnetic field B_0 which is usually along the z-axis.

The magnetic moment (μ) of a nucleus is related to its spin by the equation:

$$\boldsymbol{\mu = \gamma S} \qquad \textbf{3.3}$$

where γ is the gyromagnetic ratio, unique to each nucleus. S is the spin angular momentum.

With the application of the magnetic field B_0, the energy levels of the spin system split, and the nucleus is allowed to make a transition between these energy levels by absorbing or emitting energy. Due to the Boltzmann distribution, there is a population difference between parallel and anti-parallel precessing nuclei, given by:

$$\boldsymbol{n_-/n_+ = e^{-(\Delta E/kT)}} \qquad \textbf{3.4}$$

where n_- (anti-parallel) and n_+ (parallel) are the number of spins in the two energy states, k is the Boltzmann constant, T is the absolute temperature, and ΔE is the difference in the energy between the two states.

The energy of a nuclear spin state in a magnetic field is given by:

$$\boldsymbol{E = -m_I(h/2\pi)(\gamma B_0)} \qquad \textbf{3.5}$$

The energy difference between the two states is denoted as ΔE:

$$\boldsymbol{\Delta E = (h/2\pi)(\gamma B_0)} \qquad \textbf{3.6}$$

The frequency at which these transitions take place is called the resonance frequency, or the Larmor frequency (ω_0):

$$\boldsymbol{\omega_0 = \gamma B_0} \qquad \textbf{3.7}$$

After the system is excited by an external energy pulse, it gradually returns to its thermal equilibrium state. The two primary relaxation processes through which the system gets back to the equilibrium state are: spin-spin relaxation, defined by the time constant T2, and spin-lattice relaxation, defined by the time constant T1.

Spin-spin relaxation (T2), also known as transverse relaxation, involves loss of phase coherence between spins in the transverse plane (perpendicular to B_0). This occurs due to the interactions among neighboring spins which lead to local magnetic field variations. These variations cause different spins to precess at slightly different rates resulting in signal decay. Spin-spin relaxation involves energy redistribution within the spin system. The time constant T2 describes the decay of the transverse magnetization (magnetization perpendicular to the applied magnetic field).

Spin-Lattice Relaxation (T1), also known as longitudinal relaxation, involves energy transfer from the nuclear spins to the surrounding lattice (surrounding nuclei). This process is responsible for the return of spins to thermal equilibrium along the direction of the external magnetic field (B_0). The time constant T1 describes the recovery of the longitudinal magnetization (magnetization parallel to the applied magnetic field).

Determining the tissue properties and separating tissue types in MRI depends on these relaxation mechanisms. T1 and T2 relaxation times provide important information regarding the tissue's structure and help distinguish between different types of tissue by characterizing their physical properties based on the relaxation behaviors. Different tissues in the body like muscle, fat and cartilage have distinct T1 and T2 values. Fat generally has shorter T1 and T2 compared to muscle and cartilage. Cartilage has longer T2 due to its high water content. Millions of nuclei are present in a sample and each nucleus has its own magnetic property. The collective magnetic moment of all nuclear spins represents the net magnetization M. In the absence of any external magnetic field, the spins are randomly oriented and thus there is no net magnetization. When a magnetic field (B_0) is applied, the spins either align in parallel (up) or anti-parallel (down) to the

field, thus producing a net magnetization in the direction of B_0. The strength of the magnetization (M_0) is proportional to the difference in the population of spins in two energy states, with more nuclei aligning parallel to B_0. The torque generated on the spins determines the evolution of M in an external magnetic field, described by the following equation :

$$\boldsymbol{dM/dt = \gamma(M \times B)} \qquad \textbf{3.8}$$

When a 90° radio frequency (RF) pulse ($B_1(t)$) is applied to the sample at the Larmor frequency, it tips the magnetization vector M into the transverse plane. When the RF pulse is turned off, magnetization starts to relax and go back to its equilibrium state, initiating relaxation processes in the nuclear spins.

Transverse Relaxation (T2): The rate of decay of the transverse magnetization (M_{xy}) is given by:

$$\boldsymbol{dM_{xy}/dt = -M_{xy}/T2} \qquad \textbf{3.9}$$

Longitudinal Relaxation (T1): The rate of recovery of the longitudinal magnetization (M_z) is given by:

$$\boldsymbol{dM_z/dt = -(M_z - M_0)/T1} \qquad \textbf{3.10}$$

After excitation, changes in magnetization can be described by the Bloch equation:

$$\boldsymbol{\frac{dM}{dt} = \gamma(M \times B) - M_x i/T2 - M_y j/T2 + (M_0 - M_z)k/T1} \qquad \textbf{3.11}$$

The two relaxation processes can be described by the solutions to the Bloch equations, the decay of transverse magnetization and the recovery of longitudinal magnetization:

Transverse Relaxation:

$$\boldsymbol{M_{xy}(t) = M_{xy(0)} e^{-(t/T2)}} \qquad \textbf{3.12}$$

Longitudinal Relaxation:

$$\boldsymbol{M_z(t) = M_0(1 - e^{-(t/T1)})} \qquad \textbf{3.13}$$

The relaxation mechanisms are essential in understanding the contrast in MRI images. Different tissues in the body will appear brighter or darker in T1-weighted and T2-weighted images depending on their relative values (in addition to their concentrations), providing information on tissue properties for diagnostic purposes. T1 is typically longer than T2 because longitudinal relaxation involves a return to thermal equilibrium with the surroundings. Whereas transverse relaxation happens faster because it is associated with loss of phase coherence between spins which is a faster process than achieving equilibrium [46].

In MRI scans, the signal-to-noise ratio (SNR) is a key parameter that depends on factors such as the kind of nuclei used for imaging and the magnetic field strength B_0. For instance, hydrogen nuclei which are abundant in water and fat, have a high gyromagnetic ratio (~42.58 MHz/T) and are therefore suitable for use in MRI. Proton-based MRI focuses on hydrogen protons because they produce a strong signal in tissues with high water content [46]. There are also challenges present during the MRI experiments like magnetic field inhomogeneities, structural inhomogeneities in the sample, and image artifacts due to patient motion. Additionally, metal implants in the body, such as artificial joints or pacemakers can pose a risk to patients, as the strong magnetic field can interfere with the functioning of the implants or cause them to heat up [47].

3.1.1 Spin Echo Sequence and Relaxation Mechanisms

The way to carry out NMR and MRI experiments is via the application of a pulse sequence, which is the list of technical events in time. A fundamental pulse sequence in MRI is the spin echo (SE) sequence (Figure 3.1), which can be used to recover the spin phase coherence that is lost due to signal dephasing. The sequence begins with a 90° RF pulse that tips the spins into the transverse plane. Microscopic field fluctuations cause the spins to precess at different rates, which ultimately leads to a loss in phase coherence and hence signal decay. In order to recover the phase spread, a 180° RF pulse is applied which flips the spins causing the faster spins which were ahead to fall behind and vice versa. The spins are realigned (Figure 3.2) in phase to create a spin echo after a period that is equal to the gap between 90° and 180° pulses, which together are known as the echo time (TE) [48]. Signal decay in the transverse plane is due to two relaxation processes: T2 relaxation, a true transverse relaxation reflecting loss of phase coherence caused by spin-spin interactions, and T2* relaxation, occurring due to the dephasing effects caused by magnetic field inhomogeneities and tissue susceptibility. The SE sequence removes T2* dephasing and enables a more accurate measurement of T2 relaxation time [46]. T2 relaxation time is a useful quantitative biomarker in the assessment of cartilage properties.

3.1.2 Quantitative MRI and T2 Mapping of Articular Cartilage

MRI is a valuable imaging tool for the assessment of cartilage in osteoarthritis (OA) as it can detect early metabolic and structural changes in the cartilage [14, 49]. Quantitative MRI techniques, especially the use of T2 relaxation, are useful for cartilage health evaluation as they can provide vital information about water content, collagen

structure, and proteoglycan concentration in the cartilage [50, 51]. T2 relaxation measurements depend on tissue anisotropy together with collagen fiber orientation and water content.

- The increase in T2 relaxation values indicates elevated water mobility, reduction in collagen integrity, and consequently, early cartilage degradation.
- The Lower T2 values suggest a more organized collagen matrix with lesser water mobility [52, 53].

The magic angle effect is a key factor that influences T2 relaxation, a phenomenon where T2 values reach the maximum when the collagen fibers are oriented at approximately 55° to the magnetic field (B_0). Higher T2 relaxation times are achieved when the collagen fibers align at this specific angle (55°) because the dipolar interactions that shorten T2 relaxation become minimized at this orientation [54, 55].

3.1.3 MRI Imaging Parameters and Their Impact on Image Quality

The image resolution together with signal-to-noise ratio (SNR) and contrast in images gets affected by multiple MRI parameters. For better cartilage visualization and disease evaluation, MRI protocols can be improved by altering the following parameters.

- Field of View (FOV) and Matrix Size: The spatial resolution is inversely proportional to the FOV. A small FOV and large matrix can improve spatial resolution at the cost of reduced SNR and longer acquisition time.

$$\text{Resolution} = \text{FOV}/\text{Matrix} \qquad \textbf{3.14}$$

- Slice Thickness: Thick slices in 2D MRI can enhance the SNR but at the same time limit the spatial resolution in the slice direction.

- Number of Averages: Acquiring multiple averages can improve SNR, but this also results in an increase in scan time, which can be a problem in biomedical imaging.
- Repetition Time (TR) and Echo Time (TE): These parameters significantly affect image contrast; longer TE can enhance T2 contrast making it easier to differentiate tissues with different T2 relaxation times, but it can result in low SNR due to signal decay. A long TR ensures that all protons are fully relaxed, and this can improve the quality of T2-weighted images, at the cost of long experimental time.

3.2 Polarized Light Microscopy and Its Application in Articular Cartilage Imaging

Light being an electromagnetic wave is made up of oscillating electric and magnetic fields, these waves vibrate in multiple directions in natural light. When electromagnetic waves are only vibrating in one direction they are considered to be linearly polarized, to achieve this effect linear polarizers are used [56]. Anisotropic materials like biological tissues can split the polarized light into two distinct rays that move at separate velocities through birefringence. Structural organization of the material determines the degree of birefringence. After the specimen, a second polarizer known as the analyzer is placed perpendicular to the first polarizer to measure birefringence. If there is no birefringence, the light will stay polarized and the analyzer will block the light resulting in a dark image. However, if birefringence is present some light will pass through the analyzer resulting in a brighter image, the brightness of the image corresponds to the magnitude of birefringence [57].

Polarized light microscopy (PLM) is an established technique for studying the anisotropic properties of biological and non-biological materials [58]. Due to the collagen-rich composition in many connective tissues like articular cartilage and fibrocartilage, the exhibition of birefringence makes PLM a valuable tool for biomedical research [59]. PLM functions with the use of a light source, a polarizer, a rotating stage for the sample, an analyzer, and a detector (Figure 3.3). An anisotropic structure causes linearly polarized light to split into two rays (ordinary and extraordinary rays) moving at different speeds, the difference in refractive indices between these rays generates birefringence.

3.2.1 PLM in Articular Cartilage Assessment and Osteoarthritis Detection

The structure of articular cartilage exhibits anisotropic properties because collagen fibers are arranged differently throughout different zones of the cartilage, the orientation of the fibers determines the functional mechanical properties of the tissue.

- Superficial Zone: The topmost part of the tissue contains collagen fibers which run parallel to the articular surface. The arrangement of collagen fibers in this zone helps absorb shear forces and make joint movement smoother by reducing friction between bones.
- Middle (Transitional) Zone: The fibers found in this zone are randomly oriented. The middle zone distributes forces uniformly in the cartilage.
- Deep Zone (Radial zone): The fibers found in this zone are perpendicular to the articular surface. The deep zone supports the weight of the body and helps cartilage to hold its structure [60].

PLM provides quantitative measurements of birefringence related to the density and organization of collagen fibers. In our laboratory, the PLM instrument generates two quantitative images, which are:

- Retardation Maps: Represent the organization and density of the collagen fibers, higher birefringence measurement indicates a better organized ECM.
- Azimuth (Angle) Maps: Represent the averaged orientation of the collagen fibers. In healthy cartilage, fibers in the superficial zone are perpendicular to the fibers in the deep zone, confirming the characteristic structure of the cartilage [61, 62].

In cartilage affected by osteoarthritis, there is a loss of collagen organization which leads to structural and biomechanical degradation. PLM is highly useful in detecting these degenerative changes in the osteoarthritic cartilage. Decreased retardation values in the osteoarthritic cartilage reflect the breakdown of the collagen network and increased tissue degradation [63].

3.3 X-ray Computed Tomography

Computed Tomography (CT) operates as a non-invasive diagnostic tool which produces cross-sectional images of the body through X-ray attenuation. The imaging process of CT depends on how X-rays penetrate different materials at different depths. Medical imaging utilizes X-rays as electromagnetic radiation typically between 30 keV and 150 keV energy range. When X-rays pass through a material they are absorbed or scattered due to interactions with atoms by means of attenuation, occurring through the photoelectric effect and Compton scattering. The process of X-ray attenuation causes X-rays to lose intensity during travel through a material. The X-ray absorption properties of materials depend on their atomic number, higher atomic number materials produce better

image contrast through increased attenuation. The equation that mathematically describes X-ray attenuation:

$$I = I_0 e^{-(\mu x)} \qquad \textbf{3.15}$$

where I is the detected X-ray intensity, I_0 is the initial intensity of the X-ray source, μ is the linear attenuation coefficient of the material, and x represents the thickness of the sample.

Sir Godfrey Hounsfield established the standard for X-ray attenuation measurements through his development of the Hounsfield Unit (HU) scale. The Hounsfield Unit (HU) scale shows air at -1000 HU while water appears at 0 HU, and denser materials like bone have positive HU values [64]. The detector in CT imaging system acquires many 2D X-ray projection images from different angles which then go through advanced reconstruction algorithms like the convolution back-projection method to produce the detailed 3D structure representation of the scanned object (Figure 3.4). The role of CT imaging in diseases like osteoarthritis (OA) is valuable in assessing bone integrity and structural changes.

3.3.1 Experimental Parameters for CT Imaging

Key parameters that determine the production of high-quality CT images are:

- Voltage (kV)- This parameter controls the energy of the X-ray beam which determines its penetration depth. Higher voltage enhances X-ray penetration which makes it suitable for scanning dense materials like bones.
- Current (μA)- This parameter controls the number of X-ray photons produced. Higher current improves signal strength and image quality but increases radiation dose.

- Field of View- This parameter determines the region that is being scanned, a smaller Field of View (FOV) often results in a better spatial resolution.
- Rotation step- This parameter determines the angular increment between each acquired projection. A smaller rotation step improves image quality but increases the total scan time.
- Averages- This parameter determines the number of scans averaged per rotation step, higher averages reduce image noise and improve quality but increase the total scan time.

In CT imaging procedures, beam hardening is crucial to consider, which happens when lower-energy X-rays are absorbed more by dense materials like bones and higher-energy X-rays pass through with less absorption. The X-ray beams that reach the detector possess higher energy which generates beam-hardening artifacts that distort the image. A metal filter like aluminum is often placed between the X-ray source and the sample to minimize these artifacts. The aluminum filter helps to eliminate lower energy X-rays before they strike the sample thus reducing beam hardening effects which enhances image quality.

3.3.2 Osteoarthritis Detection Using CT Imaging

In clinical diagnostics, CT imaging functions as an essential tool to assess subchondral bone alterations in osteoarthritis (OA). During OA progression the subchondral bone experiences modifications in its structural integrity with changes in bone mineral density (BMD), volume, thickness, and porosity. During the initial phases of OA, the subchondral bone undergoes increased remodeling activity involving both resorption and formation which can result in reduced BMD [65, 66]. However, as OA

advances subchondral bone becomes thicker and is known to develop subchondral sclerosis that can result in increased BMD [67]. The high-resolution imaging capability of μCT enables the detection of small changes in BMD at the onset of OA [68]. CT imaging can help clinicians and researchers to monitor disease progression and develop treatment plans for preserving joint health.

3.4 Inductively Coupled Plasma (ICP) - Optical Emission Spectroscopy (OES)

The Inductively Coupled Plasma (ICP) technique measures the elemental composition in a sample using a spectrometer and high-temperature plasma which is typically generated by ionizing argon gas with radio frequency (RF) electromagnetic field. The plasma with extreme heat (~6000-10000K) excites the atoms in the sample, causing their electrons to jump to higher energy levels. The emission from the elements is due to the relaxation of these electrons which release photons when they return back to lower energy states. The light emitted by each element in the sample is at a characteristic wavelength and the intensity of the light is directly proportional to the concentration of the element present in the sample [69]. The measurement of elemental concentration relies on comparing the light emission intensity to standard reference values. ICP-OES operates as an efficient analytical technique which works across multiple applications including clinical diagnostic testing.

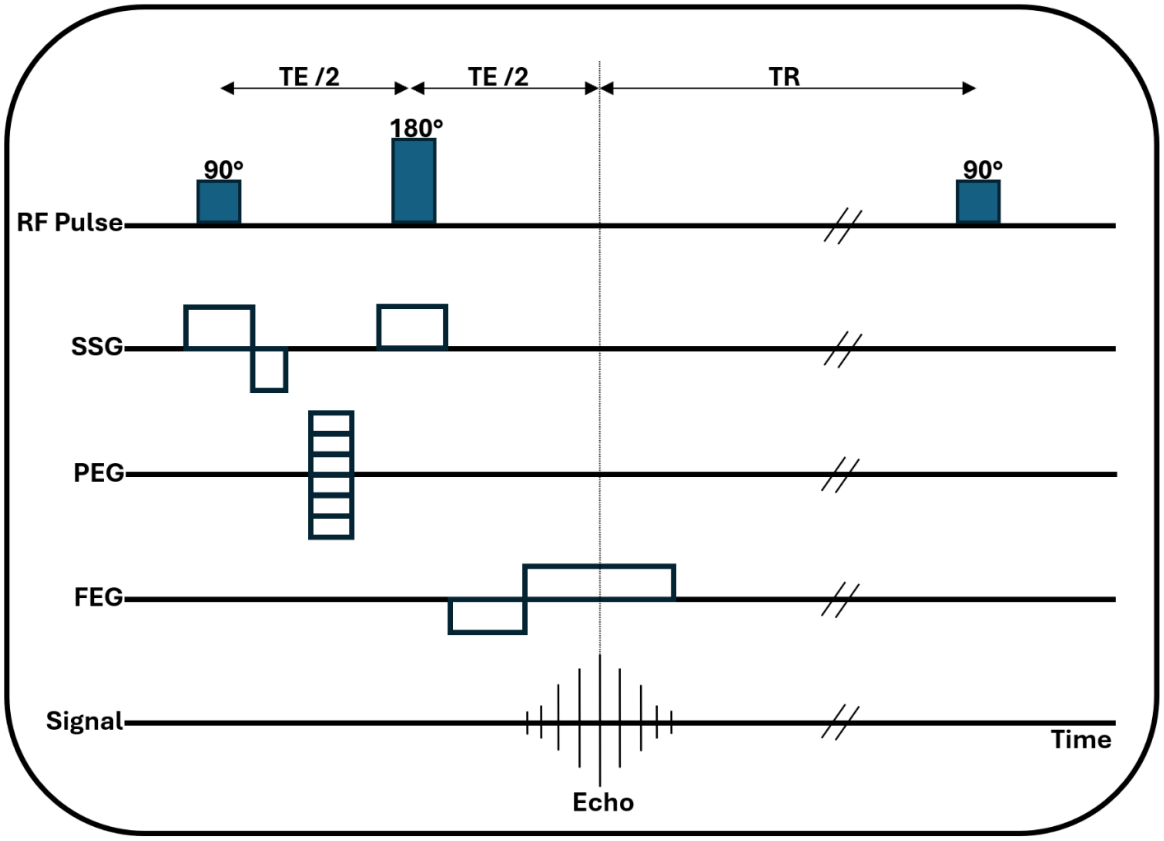

Figure 3.1 A pulse sequence diagram of a spin echo (SE) sequence is shown with timing parameters, radio frequency (RF) pulses, and gradient events. The diagram shows the repetition time (TR), echo time (TE), 90° and 180° RF pulses, and the corresponding gradients: slice selection gradient (SSG), phase encoding gradient (PEG), and frequency encoding gradient (FEG). The resulting echo signal is also shown in the diagram.

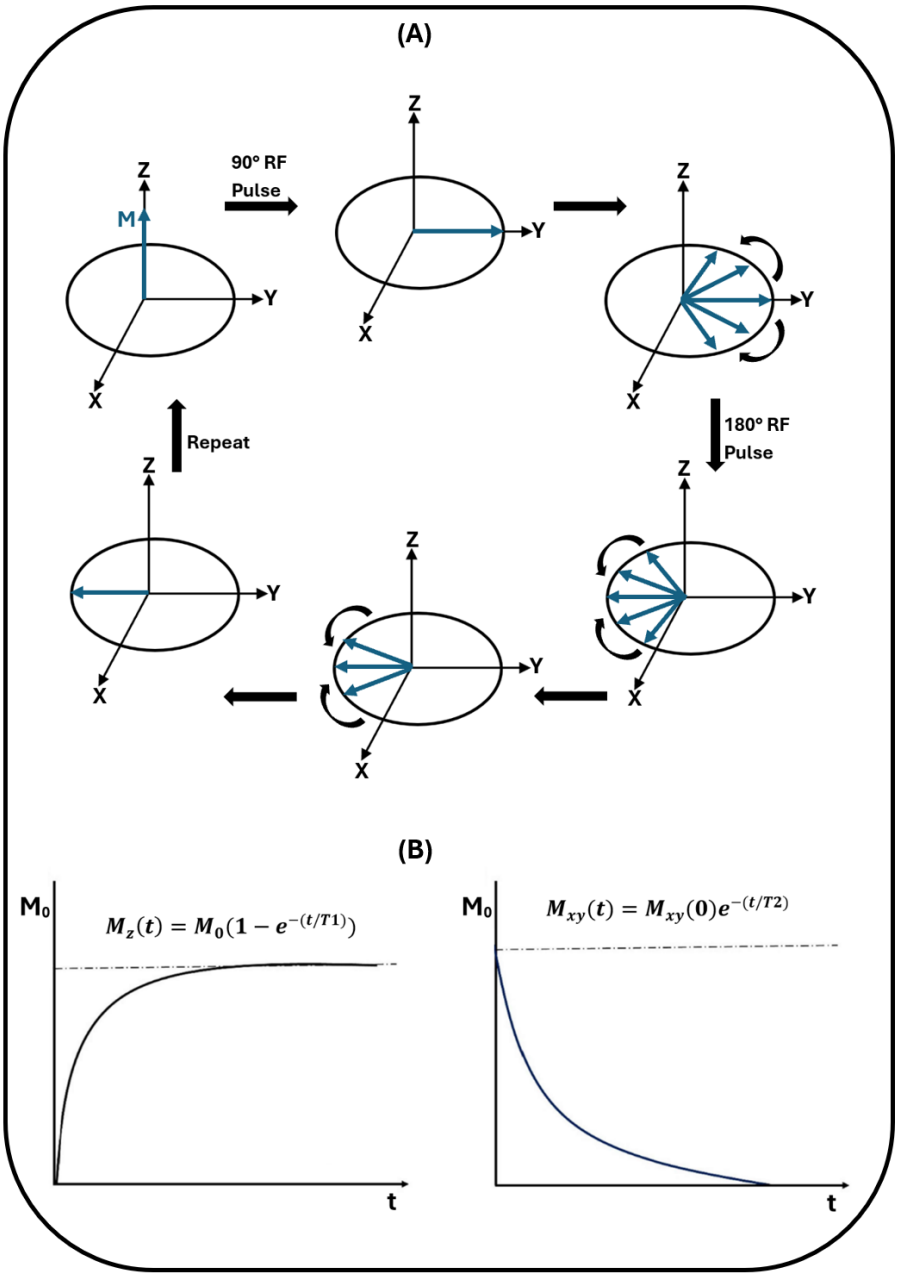

Figure 3.2 Illustration of the relaxation dynamics during the spin echo sequence. **(A)** The sequence of events in a spin echo MRI experiment is illustrated by this diagram. The net magnetization vector (M) starts along the Z-axis before a 90° RF pulse tips it into the transverse (XY) plane. The transverse magnetization undergoes dephasing, and a 180° RF pulse is applied to refocus the spins which results in the formation of a spin echo. **(B)** Graphs representing the relaxation processes: longitudinal relaxation (T1 recovery) and transverse relaxation (T2 decay).

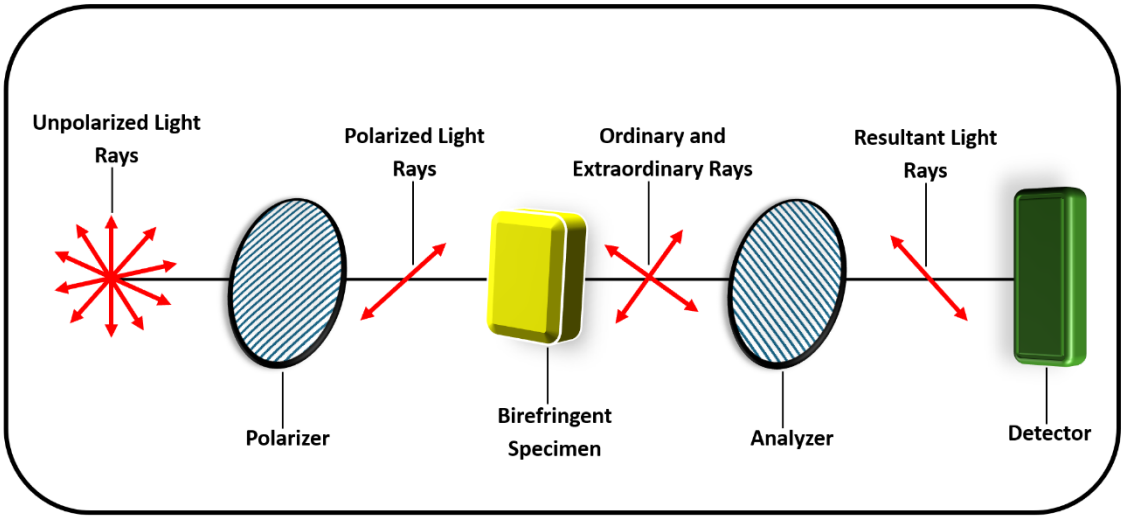

Figure 3.3 Schematic representation of the working principle of polarized light microscopy (PLM). Polarized light passes through a birefringent sample, causing changes in the light's phase. These changes are picked up by the analyzer and shown as visible differences at the detector.

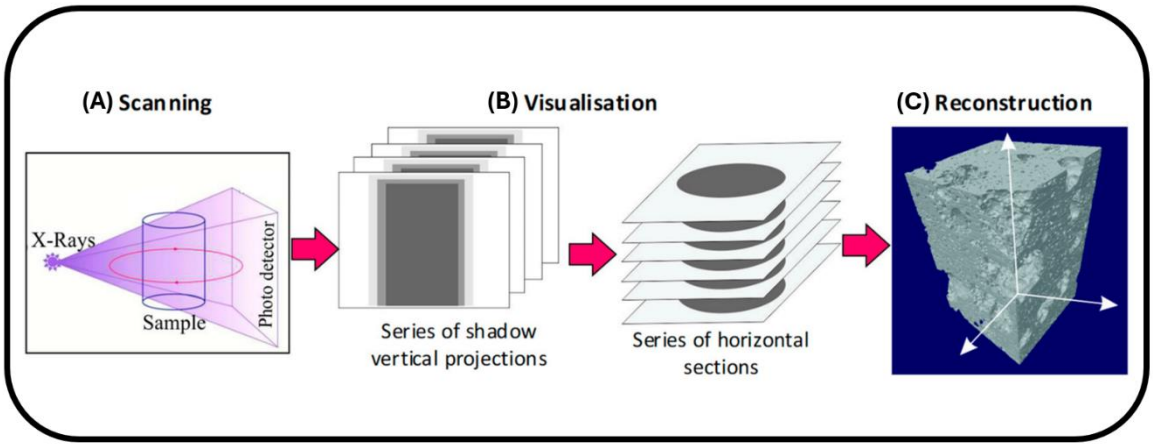

Figure 3.4 Schematic representation of the working principle of computed tomography (CT) imaging. **(A)** The sample is scanned using X-rays. **(B)** Processing of projection data using mathematical algorithms to produce horizontal slices. **(C)** Reconstructed three-dimensional image of the sample. Reprinted from [70], with permission.

CHAPTER FOUR

MATERIAL AND METHODS

4.1 Sample Preparation

The studies in this dissertation used a total of 30 mature New Zealand White female rabbits, each was around 9 months old and weighed approximately 3-4 kg at the time of the surgery. All of the animal procedures in this study were approved by the institutional review committee (IACUC: AL-2021-07). The impact surgery on the rabbit femur was performed by a surgeon on the operating table using a limb clamp and a custom-built device [71] which had a metal indenter tip with a diameter of 3 mm. Under anesthesia, the impact was applied one time to the right femoral medial condyle of each animal, at a location that was approximately equidistant from the anterior and posterior ends. The impact force was approximately 30 MPa, calibrated with the use of sensor films (Fujifilm Prescale, Sensor Products Inc., Madison, NJ). This injury was deliberately designed to be subcritical, mimicking a non-catastrophic trauma that avoids cartilage penetration and bone fracture. Such injuries occur more frequently during daily activities and can often be overlooked but may initiate degenerative changes over time. We applied this subcritical injury to induce minor joint damage, aiming to understand how such trauma affects the articular cartilage and subchondral bone, and to explore the relationship between mild mechanical injury and joint health. The left femoral medial condyle of the animal was kept unoperated to serve as a contralateral control. After receiving the impact, the rabbits were allowed to engage in normal activities without any restrictions until reaching their assigned euthanasia time points, which were 0, 2, 6, and

14 weeks post-impact; each time point had six animals. Additionally, a separate group of six animals underwent impact surgery with an approximate impact force of 65 MPa and was sacrificed at 6 weeks. This group was specifically designed to compare to the 6-week/30-MPa group to assess how an increased force influences the severity of joint damage. This comparison helped us to investigate the connection between impact intensity and cartilage damage in the joint. Across the five groups, there were a total of 60 knee samples (n=30 non-impact; n=30 impact). For the first phase of the project, following sacrifice, the rabbit whole knee joints were imaged by microscopic magnetic resonance imaging (μMRI) and microscopic computed tomography (μCT).

After the whole knee imaging, further analysis was done on the extracted cartilage-bone blocks from 2 and 14-week animal groups. Figure 4.1 shows the specimen location for the μMRI cartilage-bone block. Two cartilage-bone blocks each about 2×2×3 mm^3 in size were harvested, one from each femoral medial condyle of the non-impact and impact knee, with both taken from the matched impact locations. This resulted in n=12 blocks for the 2-week group (n=6 non-impact, n=6 impact), and n=12 blocks for the 14-week group (n=6 non-impact, n=6 impact). In the second phase of the project, cartilage blocks from the medial femoral condyle at 2 and 14 weeks post-surgery following a 30 MPa impact were examined to assess zonal changes in the cartilage. To preserve tissue integrity, the cartilage-bone blocks were bathed in the saline solution with protease inhibitors (PI). In addition to the tissue blocks from the impact location for μMRI imaging, cartilage tissues were harvested from the adjacent anterior and posterior portions of the femur for biochemical analysis shown in Figure 4.1. These samples were

analyzed using the Inductively Coupled Plasma (ICP) technique to determine the water (H_2O) and glycosaminoglycan (GAG) contents.

In the third phase of the project, cartilage-bone blocks from the femoral condyle at 2 and 14 weeks post-surgery were further analyzed to detect microstructural alterations using polarized light microscopy (PLM) and microscopic computed tomography (μCT) imaging. In addition to the blocks from the impact location for PLM and μCT imaging, cartilage samples from the adjacent anterior and posterior portions of the impact location were analyzed using the Inductively Coupled Plasma (ICP) technique to measure calcium content in the calcified zone of the cartilage.

4.2 Microscopic Magnetic Resonance Imaging Protocols

For the first phase of the project, all the unopened knees were imaged using a μMRI instrument, a Bruker AVANCE III HD 300 spectrometer equipped with a 7-Tesla vertical bore magnet (Bruker, Germany). The multi-echo pulse sequence was used for quantitative imaging of the rabbit whole knee joints. The field of view was 28×28 mm, which yielded an initial pixel size of 109 μm. During post-processing, the raw images were reconstructed from an initial matrix size of 256×256 to a higher matrix size of 512×512, resulting in a final pixel size of 55 μm [72]. The experimental parameters were: repetition time (TR) of 3.5 s, slice thickness of 0.8 mm, 6 signal averages, and echo time (TE) of 6.7 ms. The echo times began at 6.7 ms and incremented by 6.7 ms for each subsequent echo, for a total of 5 echoes (i.e., five intensity images, each acquired at a different echo time). Each set of the five intensity images was used to evaluate the signal decay at different echo times, which enabled the construction of one quantitative T2 relaxation image. The total scanning time for each joint was 1 hour and 30 minutes.

For the second phase of the project, extracted cartilage-bone blocks from 2 and 14-week animal groups were imaged using a 3 mm solenoid coil for quantitative MRI T2 imaging on the same Bruker μMRI system with a 7-Tesla vertical bore magnet (Bruker, Germany). The specimens were imaged at two different orientations, 0° and 55° to the external magnetic field B_0, which were necessary to study deeper regions in cartilage [54, 73]. Dipolar interactions in cartilage are minimal at 55° (the magic angle), which results in a homogenously laminated appearance of cartilage in the images that is more useful for visualizing cartilage degradation in the deeper zones. This is in contrast to the 0° orientation at which cartilage displays an anisotropically laminated appearance due to greater dipolar interactions [54, 73, 74]. The quantitative imaging used a field-of-view of 3×3 mm^2 with a slice thickness of 0.8 mm and an acquisition matrix of 256×128, which was later reconstructed to a 256×256 matrix, resulting in a transverse resolution of 11.7 μm/pixel. The repetition time for the experiments was 1.8 s. The T2-weighted images were acquired at four echo times (2, 4, 6, and 12 ms) using the CPMG magnetization-prepared imaging sequence with a scan time of approximately 1 hour and 30 minutes [54, 73].

4.3 Microscopic Computed Tomography Imaging Protocols

In the first phase of the project, after the μMRI experiments, the unopened whole knees from all animal groups were imaged using a μCT instrument, the Skyscan 1174 system (Bruker, Kontich, Belgium). All experimental parameters were consistent: a voltage of 50 kV, a current of 800 μA, a rotation step of 0.5°, 10 signal averages, 0.2 mm aluminum filter, and a 1024×1024 data matrix, which yielded a pixel size of 30.4 μm. The total scanning time for each joint was 54 minutes.

For the third phase of the project, extracted cartilage-bone blocks from 2 and 14-week animal groups were imaged using the same Skyscan 1174 system, where the consistent experimental settings were used for all cartilage-bone blocks: 45 kV, 700 μA, 0.5° rotation step, 10 averages, 0.2 mm aluminum filter, and 1024×1024 data matrix. The images were acquired at a high resolution of 6.7 μm and the total scanning time for each sample was 54 minutes.

After scanning, the μCT data was reconstructed using the commercial software NRecon (Bruker, Kontich, Belgium), and the reconstructed images were then analyzed for the BMD using CT-Analyser (Bruker, Kontich, Belgium). The BMD measurements in the specimens were calibrated in grams of hydroxyapatite per cubic centimeter (g/cm^3) using the density scales of the measured attenuation coefficients of standard μCT phantoms (Bruker, Kontich, Belgium).

4.4 Polarized Light Microscopy Protocols

For the third phase of the project, the cartilage-bone samples were preserved in 10% buffered formalin and transferred to an outside agency for paraffin-embedded tissue histology (Western Michigan University, School of Medicine, Kalamazoo, MI). Sections from histology with a thickness of 6 μm were imaged by the PLM system [61] comprising a digital imaging setup (Cambridge Research & Instrumentation, Woburn, MA) mounted on a polarized light microscope (Leica, Buffalo Grove, IL). The quantitative imaging was done at an objective of 10X, resulting in a resolution of 1.0 μm/pixel. For each histological section, the PLM system produced a pair of quantitative images - an optical retardation image with units of nanometers and an orientation angle

image, shown in Figure 4.2. These images were used to carry out analysis of the birefringent properties of the cartilage tissue.

4.5 Inductively Coupled Plasma Protocols

A Perkin Elmer inductively coupled plasma optical emission spectrometer (ICP-OES), Optima 7000 DV (Waltham, MA) was used to determine the elemental concentration in the cartilage block samples from 2 and 14-week animal groups using a previously established protocol [75]. The sample preparation began with the removal of bone from each cartilage-bone block. The cartilage specimens were weighed for their wet weight, after which they were placed in an oven at 90° F for three hours, the samples were then taken out of the oven and weighed for their dry weight. For the second phase of the project, the water percentage was calculated based on the two measured values of wet weight and dry weight. GAG concentration measurements were based on the ^{23}Na ICP-OES analysis, sodium was used as a surrogate marker for GAG content due to its electrostatic association with the negatively charged GAG molecules in the cartilage matrix. For the third phase, calcium concentration measurements were based on the ^{40}Ca ICP-OES analysis. Before ICP analysis, cartilage tissue was liquified overnight using concentrated 100 µl HNO_3 and then diluted to 10 ml with deionized water. Five standard solutions were also examined for calibration purposes. Previous research has discovered high concordance between MRI and ICP data [76].

4.6 Image/Data and Statistical Analysis

In the first phase of the project, post-impact cartilage damage in whole knee MRI images across all animal groups was assessed using T2 maps that were generated from quantitative 2D MRI images acquired at five different echo times. The calculation of T2

used public domain software, ImageJ (National Institutes of Health, Bethesda, MD), and was based on an exponential expression:

$$S = S_0 e^{-(TE/T2)} + C \qquad \textbf{4.1}$$

where S was the observed signal intensity, S_0 was the initial signal at the shortest echo delay, TE was the echo time, and C accounts for the background noise. In these T2 maps, the regions of interest (ROI) were created to focus on the cartilage at the impact site, to analyze the site-specific damages.

To compare the articular cartilage damage between non-impact and impact samples, the matched ROIs were also created in the contralateral, non-impact knee samples. In addition, to evaluate the spread of cartilage damage a second ROI was made in the posterior location of the femoral cartilage. Figure 4.3 shows the visual representation of these ROIs. To distinguish cartilage damage between superficial and deep tissue, the full thickness of the cartilage was divided into two equal-thickness zones within the ROIs, zone-1 spanning from the superficial layer to the midpoint of the cartilage and zone-2 spanning from the midpoint to the deeper layer where the cartilage connects to the subchondral bone. Data collected from the T2 maps was further analyzed using Microsoft Excel, where T2 relaxation values (in milliseconds) were used to evaluate the progression of cartilage damage. Measured T2 values were also used to assess the severity of damage at 6 weeks post-impact under two different impacts (30 MPa vs 65 MPa).

Reconstructed data from the μCT scans was analyzed to evaluate changes in the subchondral bone post-impact. The BMD measurements were taken from the region directly beneath the articular cartilage at the impact site. Twenty-five consecutive slices

with a total thickness of 0.76 mm (~ the same thickness of one μMRI image thickness) were analyzed for the BMD assessment. Statistical analyses of both T2 relaxation times and BMD measurements were performed using KaleidaGraph (Reading, PA). A one-way ANOVA with Bonferroni post-hoc test was conducted to compare non-impact and impact specimens across all time points (0, 2, 6, and 14 weeks), where a p-value <0.05 was considered significant.

In the second phase of the project, to study the 2D images of cartilage block samples from 2 and 14-week animal groups, T2 maps were generated using the T2-weighted intensity images at four different echo times, using a public domain software, ImageJ (National Institutes of Health, Bethesda, MD). In each T2 map, a ten-pixel wide ROI was applied to the image to generate a 1D profile along the cartilage depth which was further analyzed using Microsoft Excel. Following an established division method [61, 62], the full thickness of the cartilage was separated into three cartilage zones based on the bell-shaped curve obtained at T2-0°, the superficial zone (SZ), transitional zone (TZ), and radial zone (RZ). The RZ was further divided into equal halves RZ1 and RZ2. The total thickness of the cartilage was determined using the images obtained at T2-55°. The zonal T2 values from the 1D profiles were used to determine the degradation of impact cartilage and to compare the tissue properties between non-impact and impact specimens. For each 10-pixel wide ROI, 10 data points were created by averaging each pixel across the depth. These data points were then used for statistical analysis of T2 relaxation time. The statistical analyses were conducted on T2 relaxation times and ICP measurements using the commercial software KaleidaGraph (Reading, PA). The paired

student t-test was performed to compare non-impact and impact samples at 2 and 14 weeks, where a p-value <0.05 was considered significant.

In the third phase of the project, PLM images of the histological sections from 2 and 14-week animal groups were analyzed using ImageJ (National Institutes of Health, Bethesda, MD). A one-hundred-pixel-wide ROI was applied to the 2D optical retardation PLM images to generate a 1D profile along the cartilage depth for each sample. Optical retardation data from the 1D profile was further analyzed using Microsoft Excel to compare non-impact knee (NIK) and impact knee (IK) samples. To analyze optical retardation in different regions of the tissue, the depth of the cartilage was divided into four tissue regions: superficial zone (SZ), transitional zone (TZ), radial zone (RZ), and calcified zone (CZ), using the established criteria [61, 62]. Reconstructed data from the μCT scans was analyzed using CT-analyzer (Bruker, Kontich, Belgium) software. The subchondral bone plate (SBP) region was analyzed for BMD measurements, from the start of the SBP region, in each sample, a total of 100 axial slices along the depth were analyzed for mean BMD value in g/cm^3. The depth of the SBP region was approximately 0.67 mm, which was equally divided into two regions (region-1 and region-2) of 50 slices each, and mean BMD was measured from each region. The statistical analyses were conducted on optical retardation, BMD, and ICP measurements using the commercial software KaleidaGraph (Reading, PA). The paired student t-test was performed to compare non-impact and impact samples at 2 and 14 weeks, where a p-value <0.05 was considered significant.

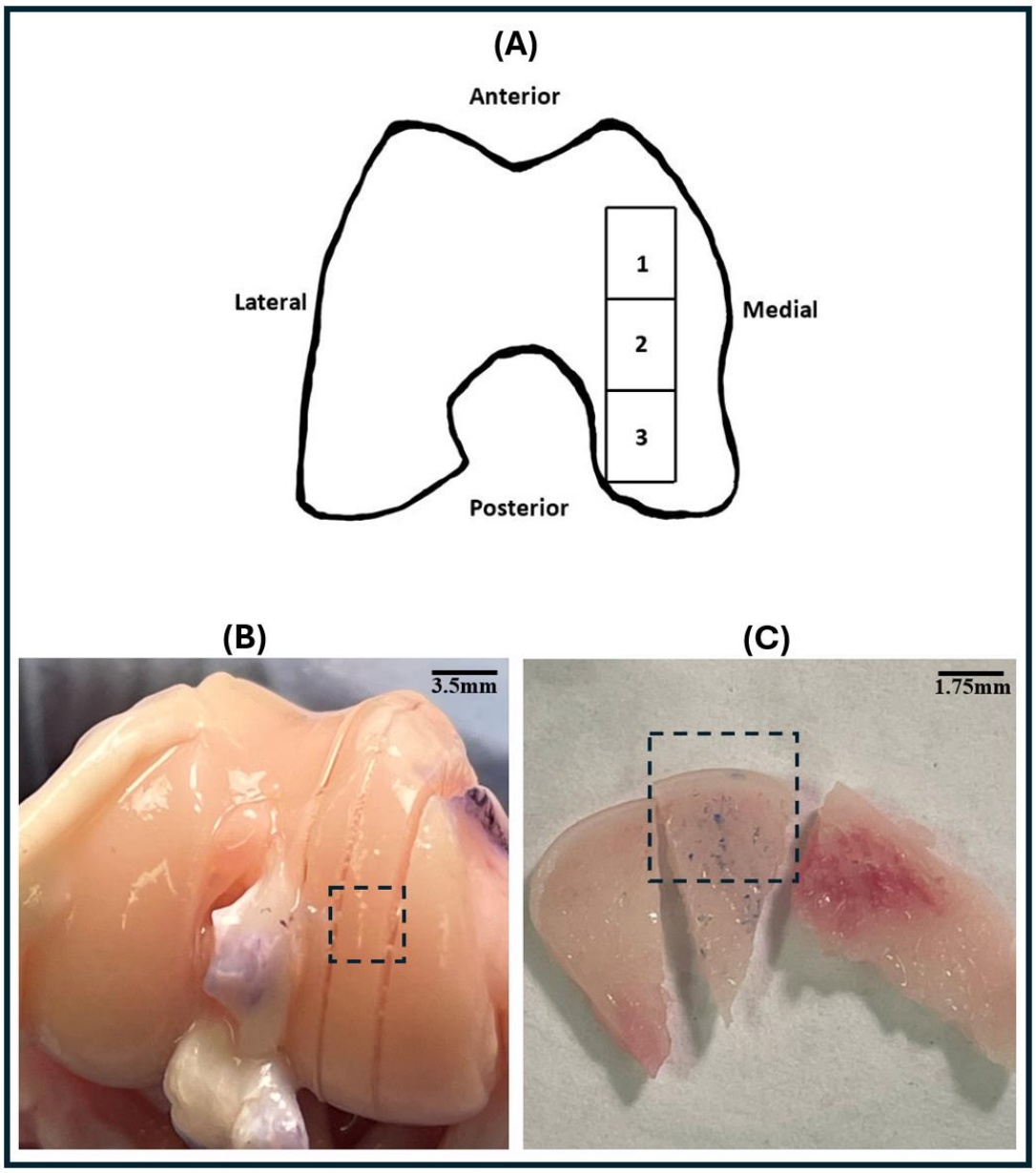

Figure 4.1 (A) Specimen locations for the μMRI and ICP experiments, which were used for quantitative analysis of T2 and compositional measurements. The central specimen (#2) was studied individually in μMRI and the adjacent specimens (#1 and #3) from the anterior and posterior portions of the AC were evaluated using biochemical analysis. **(B)** Photograph of the cut femoral slice, with a dotted box indicating the region on the medial side where the cartilage block was extracted. **(C)** Photograph of the harvested cartilage-bone specimen prepared for μMRI imaging.

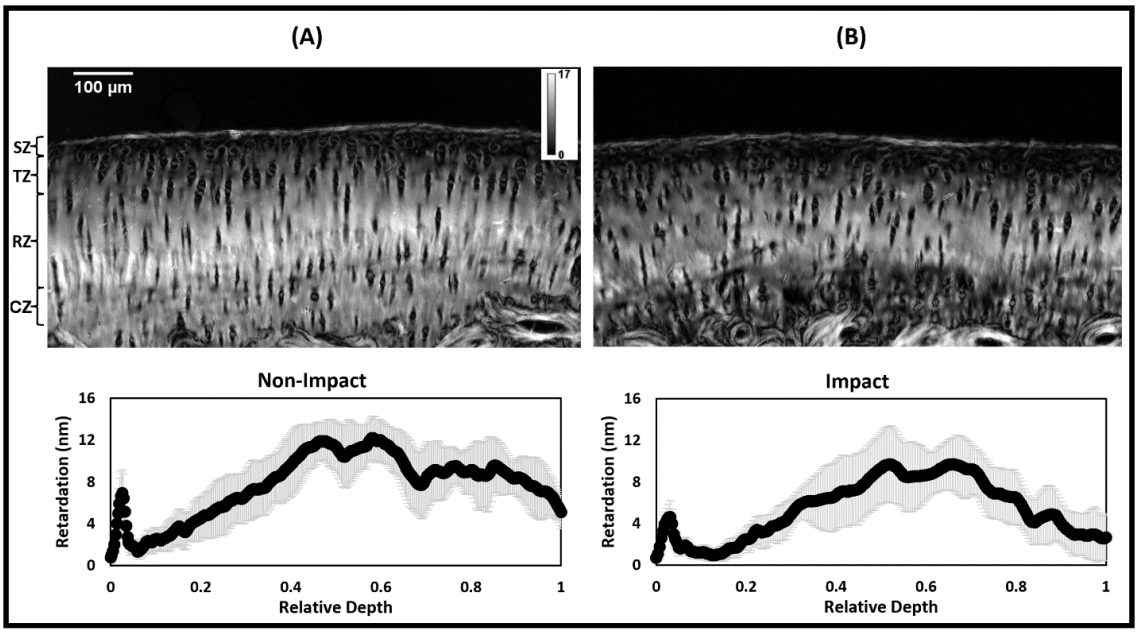

Figure 4.2 Representative set of 2D quantitative optical retardation PLM images along with their associated depth-dependent profiles (in unit of nm) from rabbit knee articular cartilage at 1µm/pixel resolution. The profiles also contain the standard deviations. **(A)** Shows the optical retardation image and its profile from a non-impact sample at 14-week time point, including the depth-wise zonal divisions of the cartilage and the retardation scale. **(B)** Shows the optical retardation image and its profile from an impact sample at 14-week time point.

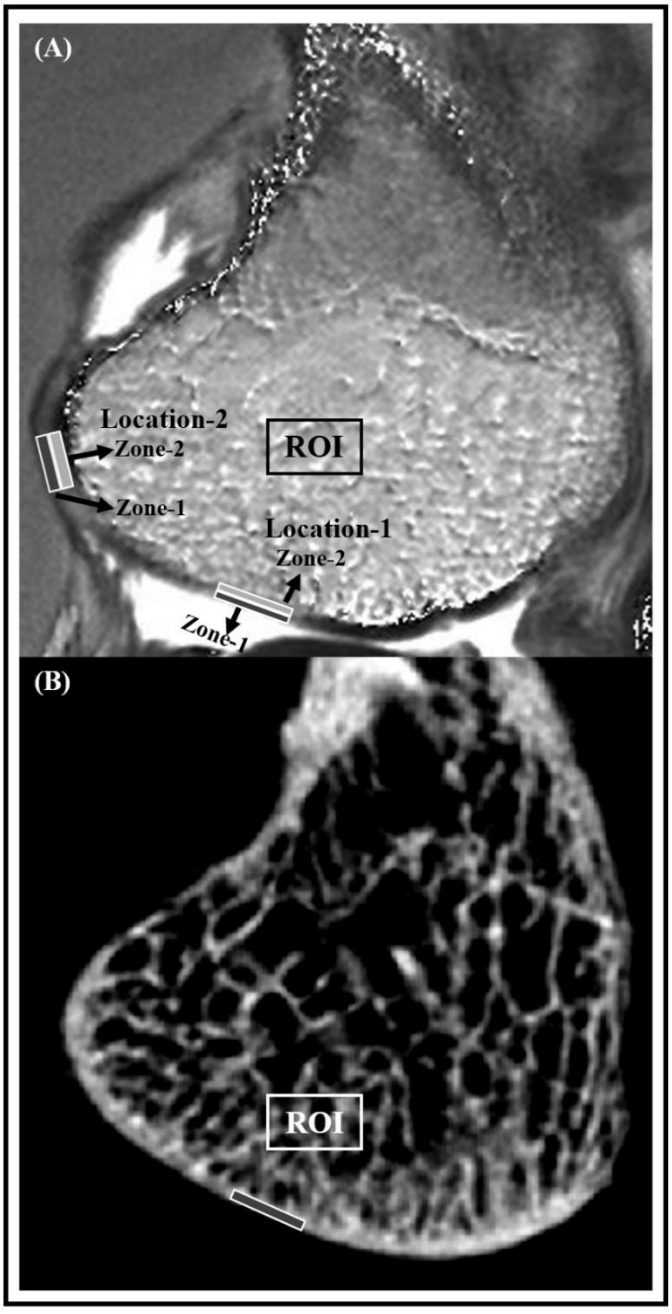

Figure 4.3 Illustration of the regions of interest: **(A)** μMRI T2 image highlighting the depth-dependent zones at Location-1 (impact site) and Location-2 (posterior region of the femur); **(B)** μCT image depicting the subchondral bone region beneath the impact cartilage, where BMD measurements were conducted.

CHAPTER FIVE

PROGRESSION OF POST-TRAUMATIC OSTEOARTHRITIS OVER 14 WEEKS FOLLOWING A SUBCRITICAL INJURY

5.1 Introduction

Degradation of articular cartilage and remodeling of subchondral bone are the typical hallmarks of post-traumatic osteoarthritis (PTOA). A direct mechanical impact on the joint can damage the cartilage matrix and cause chondrocyte death, all leading to a gradual reduction in the joint's ability to support weight and movement. For accurately understanding the early stages of PTOA formation and articular cartilage deterioration, animal models are highly advantageous [54, 77], since a particular event can be initiated in the animals and any subsequent changes can be monitored with different tools and methods [78].

Since water is the major component in connective tissues including cartilage, magnetic resonance imaging (MRI) is the best non-invasive imaging technique to observe early degradation of the AC [79, 80]. Among all MRI parameters, T2 relaxation time is extremely useful for assessing cartilage health as it is highly sensitive to water motion [54]. Higher T2 values in the diseased cartilage signify greater water content in ECM, disrupted collagen network, lower proteoglycan content, and weaker interactions between water and the macromolecules in cartilage [81-83]. Since an increase in free water motion in the degraded cartilage leads to higher T2 relaxation time, the MRI signal is greater for the water molecules that are freer in their motion than the water molecules that are tightly attached to the macromolecules via intermolecular interactions.

In this study, we tracked the progression of PTOA in the rabbit model following a single direct impact on the femoral articular cartilage. In the first phase of this project, the objective was to track femoral cartilage degradation from 0 to 14 weeks after mechanical injury and to assess how variations in injury duration and force magnitude influence cartilage damage and the development of PTOA. Using μMRI and μCT, we monitored the changes in cartilage and subchondral bone over 14 weeks. The experimental protocols have been presented in the previous Chapter, Chapter Four.

5.2 Results

Figure 5.1 illustrates the differences in the T2 images between the non-impact and impact joints at 14 weeks post-impact. Visible differences are noticeable in the color T2 images (lower row), where the impact cartilage had higher values of T2 relaxation times in the regions where the impact occurred. In MRI, higher T2 values in cartilage are commonly related to soft-tissue damage, for example, more water content, freer water molecules, and fewer macromolecules (proteoglycans).

These visual observations on the T2 maps were supported by the quantitative analysis of the T2 values. Figure 5.2 contains the zonal-specific T2 relaxation times in cartilage among all time points and all comparisons at Location 1 (the impact site). Several observations can be made in Figure 5.2A, which has the T2 values from cartilage at zone 1, the surface half of the tissue at the impact location. First, the five sets of non-impact tissues over the duration of 14 weeks, although showed a small increase gradually over time, had no statistical differences among their values. This insignificance showed that the T2s in the non-impact tissues stayed approximately constant over the 14 weeks. Second, five sets of impact tissues over the duration of 14 weeks showed steady increases

in their T2 values, where the differences between the non-impact and impact tissues became statistically significant for the last two groups (6-week high impact, 14-week). Third, compared with the zero-week impact tissues, the impact tissues at 6-week, 6-week high-impact, and 14-week all had statistically significant increases in T2 values. Fourth, each box plot in Figure 5.2A was the average of six different animals. When comparing the variations among the box plots, the T2 variations in the impact animals were bigger than the non-impact animals. This difference may point out the fact that the progression of tissue degradation varied among animals in the same group, even though all underwent the same procedure. Some animals exhibited faster degradation, while others progressed slowly. Finally, comparing two groups at 6 weeks, the group of rabbits that received an impact of 65 MPa demonstrated higher T2 changes between non-impact and impact knees compared to the 30 MPa group; the changes in the high-impact group were statistically significant while the changes in the low impact group were not. This demonstrates that the extent of impact is proportional to the amount of tissue damage.

Figure 5.2B has the T2 data from cartilage at zone 2, the deep half of the tissue at the impact location. Compared with the upper half of the cartilage, all T2 values in zone 2 were lower than zone 1, which agrees with the depth-dependent T2 profiles observed at high resolutions [84]. Apart from that difference, most of the observations found in Figure 5.2A can also be noticed in Figure 5.2B. For example, the impact cartilage had higher T2 values than their corresponding non-impact samples; the amount of T2 increases were related to the post-surgery weeks; and there were larger variations in T2 among the impact animal groups. Several comparisons were found to be statistically significant, as shown in Figure 5.2B.

We also carried out an identical analysis for cartilage in Location 2, the posterior region of the femur cartilage, away from the impact site. No prominent T2 changes were noted for any groups at Location 2. This difference between Location 1 and Location 2 highlights the site-specific nature of the post-traumatic damage. The data collectively suggest that, at least during the initial stages, cartilage damage after subcritical trauma remained localized to the impact site. All data are summarized in Table 5.1.

A correlation analysis between the non-impact and impact samples is shown in Figure 5.3, which compares the effects of two different impact forces at 6 weeks. Since the dotted diagonal line in the center has a slope of 1, any data point above the diagonal line has a higher T2 post-impact. Figure 5.3 shows that all T2 values in the impact tissue had higher T2 than the non-impact tissue. In addition, the T2 values in the tissue subjected to high impact (65 MPa) were greater than those in the low-impact (30 MPa) group, as indicated by the fitted solid slope lines, which were steeper for the 65 MPa group compared to the 30 MPa group. This illustrates that the higher impact force led to greater damage in both cartilage zones at the impact location.

At early time points (0, 2, and 6 weeks), no prominent changes in the BMD were observed between non-impact and impact samples. The absence of any major alterations in BMD may suggest that subchondral bone remodeling progresses slower than cartilage degradation. By 14 weeks, lower BMD values were observed in the impact knees compared to non-impact knees, with a difference of nearly 5%. While this difference was small, it may hint at the start of potential bone remodeling beneath the diseased cartilage. The BMD data suggests that the subchondral bone remained stable during the early

stages of PTOA progression compared to cartilage deterioration after a subcritical impact injury. The BMD measurements are summarized in Table 5.1.

5.3 Discussion

The progression of post-traumatic osteoarthritis (PTOA) was studied in a rabbit model following a subcritical injury to the femur articular cartilage. Integrating MRI T2 mapping with the subchondral bone BMD analysis in this study helped to better understand the early cartilage damages and the time-dependent nature of PTOA progression.

The gradual increase in the T2 values at the impact site over time highlighted the progressive nature of cartilage damage, following a mechanical injury. By 14 weeks, T2 values at the impact site saw a significant increase of 28% in Zone-1 (surface tissue) and 30% in Zone-2 (deep tissue) when compared to the non-impact knee samples. Both zones showed similar increases in T2 values reflecting consistent cartilage changes across cartilage depth suggesting the cartilage damage was not just superficial deterioration. In addition, progressive increases in T2 relaxation time following a mechanical injury have been reported in prior animal model studies [85-87]. The lack of significant T2 changes in the posterior location (Location-2) suggests that the trauma-induced damage remained localized to the impact region during the early stages. Although quantitative analysis captures cartilage degradation more accurately, qualitative visualization using T2 maps provides a quick overview of the increased T2 values in the impact knees.

Three features in this μMRI data are worth pointing out. First, our data in Figure 5.2 demonstrates increasing differences in the quantitative T2 values between non-impact and impact samples over the course of post-surgery weeks and variations within the

impact groups. These variations in the box plots emphasize that, even in a highly controlled animal model study, there are variations in tissue degradation among individual animals. We suspect a similar situation exists in humans too, which contributes to the challenges of early diagnosis of osteoarthritis. Second, cartilage damage observed at 6 weeks after receiving impact at 30 MPa and 65 MPa highlighted the relationship between injury severity and cartilage degradation. Significantly higher T2 values observed in the 65 MPa group suggest that injury at higher magnitudes can play a role in accelerating cartilage deterioration. Finally, most of the T2 changes were from the impact site, not in the surrounding tissues, which highlights a delayed spreading of tissue degradation, gradually from the impact site toward the surrounding tissues.

In a related study [88] which was conducted as a part of this multi-aim project, cartilage blocks were harvested from the impact region and high-resolution μMRI was carried out at 11.7 μm pixel size. This fine-resolution approach enabled the zonal T2 analysis and differentiation between individual depth-dependent layers in cartilage, such as superficial, transitional, radial zone-1, and radial zone-2. The results from the cartilage block study showed similar trends to the whole knee imaging, with elevated T2 values in the impact knees compared to the non-impact knees at the respective time points. High-resolution μMRI allows for a detailed assessment of the cartilage and can capture subtle changes within specific zones. Such fine-resolution imaging particularly helps to understand the depth-dependent progressive nature of cartilage deterioration, where prior studies have shown that injury-related cartilage damage progresses from the superficial zone to deeper layers [52]. While high-resolution μMRI imaging captures fine details, it is time-consuming and examines only a tissue block. In contrast, whole-knee imaging

helps in retaining the structural and biochemical integrity of the cartilage by imaging it intact with the joint in its natural environment, at a relatively lower resolution. Whole-knee imaging is thus useful in providing quick insights into disease progression while preserving tissue's integrity making it an effective and non-invasive option for conducting long-term studies on a subject. The whole joint imaging using an animal model can also serve as a translational bridge between μMRI and clinical MRI of human subjects that has even coarser resolution [77].

The BMD measurements of the subchondral bone beneath the impact cartilage revealed minimal to no changes during the initial stages of this study. Only a difference of 5% was measured at a 14-week time point with lower BMD in the impact samples compared to the non-impact samples. The lack of significant alterations in the subchondral bone reflects the early-stage response to a subcritical injury. It might indicate that early PTOA due to subcritical trauma likely begins with cartilage deterioration before progressing to bone remodeling at later stages [67, 89, 90]. Future studies with extended follow-up measurements could provide better insights into the relationship between subchondral bone remodeling and mechanical injuries.

5.3.1 Limitations

Twelve adult female NZW rabbits were used in our animal procedures. All left femoral heads remained unimpacted and each right femoral medial condyle was impacted once. We cannot completely rule out the possibility of surgical stress contributing to cartilage deterioration since our study lacks sham surgery on the non-impact knee. This choice of using a contralateral control limb in place of a sham group or sham limb was made tactically to drastically lower the number of rabbits needed for our research and

spare the animals from the excruciating pain and suffering associated with bilateral surgical procedures which was a requirement suggested by the institutional review committee. Any inconsistency in impactor or limb positioning or rigidity during impact could theoretically have led to differences in impact energy between animals, however, we took numerous precautions to limit variability and maximize consistency between impacts. We conducted this study using a validated impactor device [91] which utilized a spring-loaded weight for consistent impact force and velocity, and surgical limbs were rigidly mounted to the impactor frame via an intra-op k-wire to maximize rigidity for consistent transmission of force from the impactor to the articular surface. Furthermore, multiple hardware interlocks allowed the impactor device to be rigidly affixed once positioned on the femoral surface, ensuring rigidity during the impact event. Availability of male rabbits was extremely low for the experiments that were conducted during the COVID-19 pandemic hence we limited our investigation to using only female rabbits, and therefore we are unable to assess potential sex differences in response to subcritical impact injury. All rabbits were randomly assigned to different groups and were monitored carefully. No specific trends related to age or weight were observed during the progression of degradation from the impact.

5.3.2 Conclusion

This study highlights the importance of MRI T2 mapping as a powerful tool for both clinical and research settings, to monitor cartilage degradation over time following a mechanical injury. Four findings from this quantitative MRI T2 study are worth mentioning: longer duration after the trauma results in greater degradation, a higher impact leads to more degradation, noticeable degradation variations in the same group of

impact animals, and initial degradation in cartilage only detectable at the impact site. We show that quantitative μMRI data can be highly useful for identifying subtle degenerative changes in cartilage before major morphological and structural changes occur in the joints. In cases of a minor trauma, the damage can go undetected in routine clinical diagnosis which can lead to the onset of PTOA. Diagnosing tissue degradation in the early stages can help develop therapeutic interventions to slow or halt the progression of PTOA and prevent long-term or permanent joint damage. Future research should focus on investigating treatment options that help in slowing down the development of PTOA in its early stages. This study is currently under peer review for publication in Magnetic Resonance Imaging.

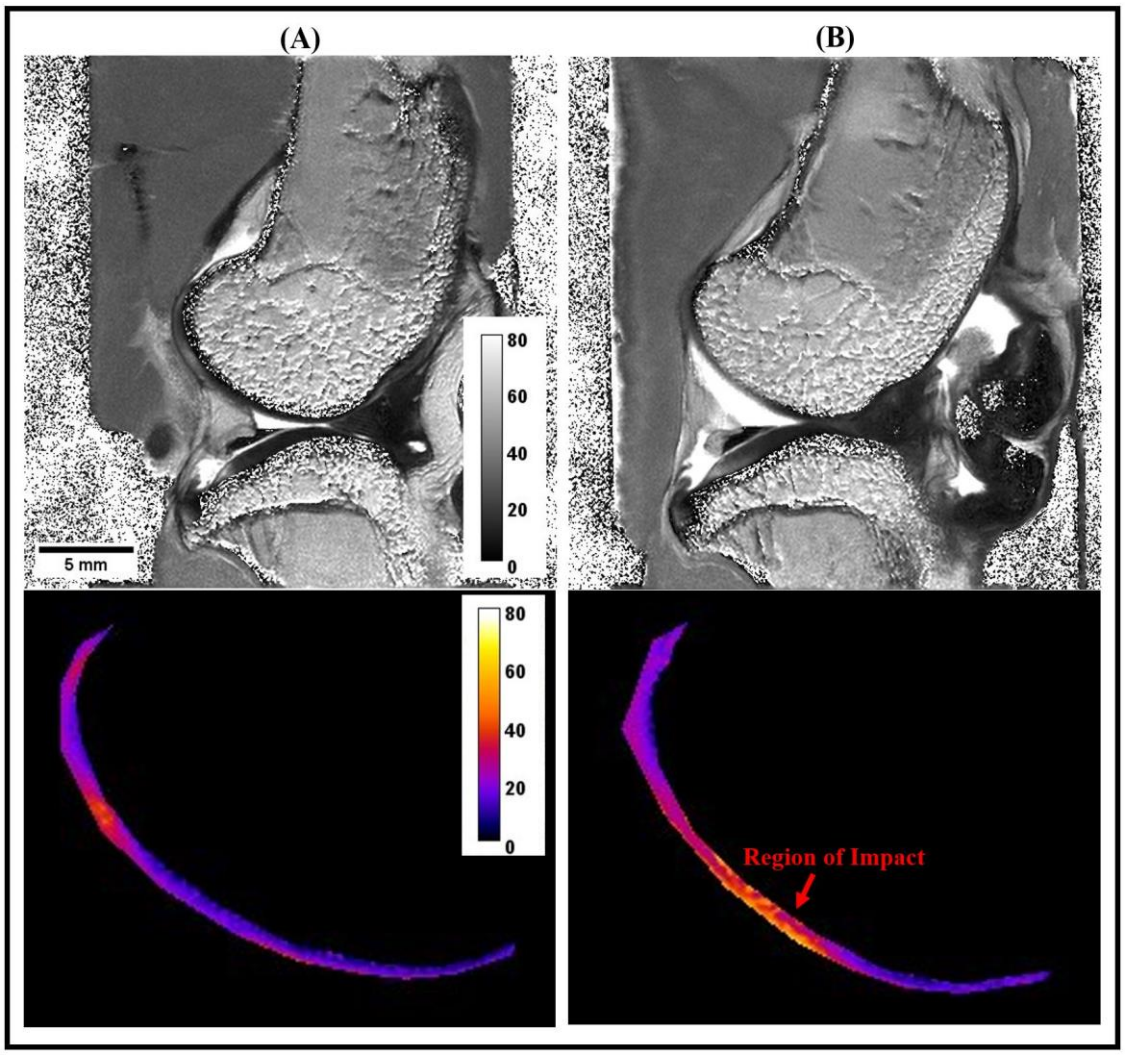

Figure 5.1 Representative MRI T2 maps of knee imaged at 14 weeks post-impact: **(A)** Non-Impact and **(B)** Impact. Below each main grey-scale image, the colored T2 maps of cartilage provide a zoomed-in view of the soft tissue. The hotter color (Orange) represents more cartilage degradation.

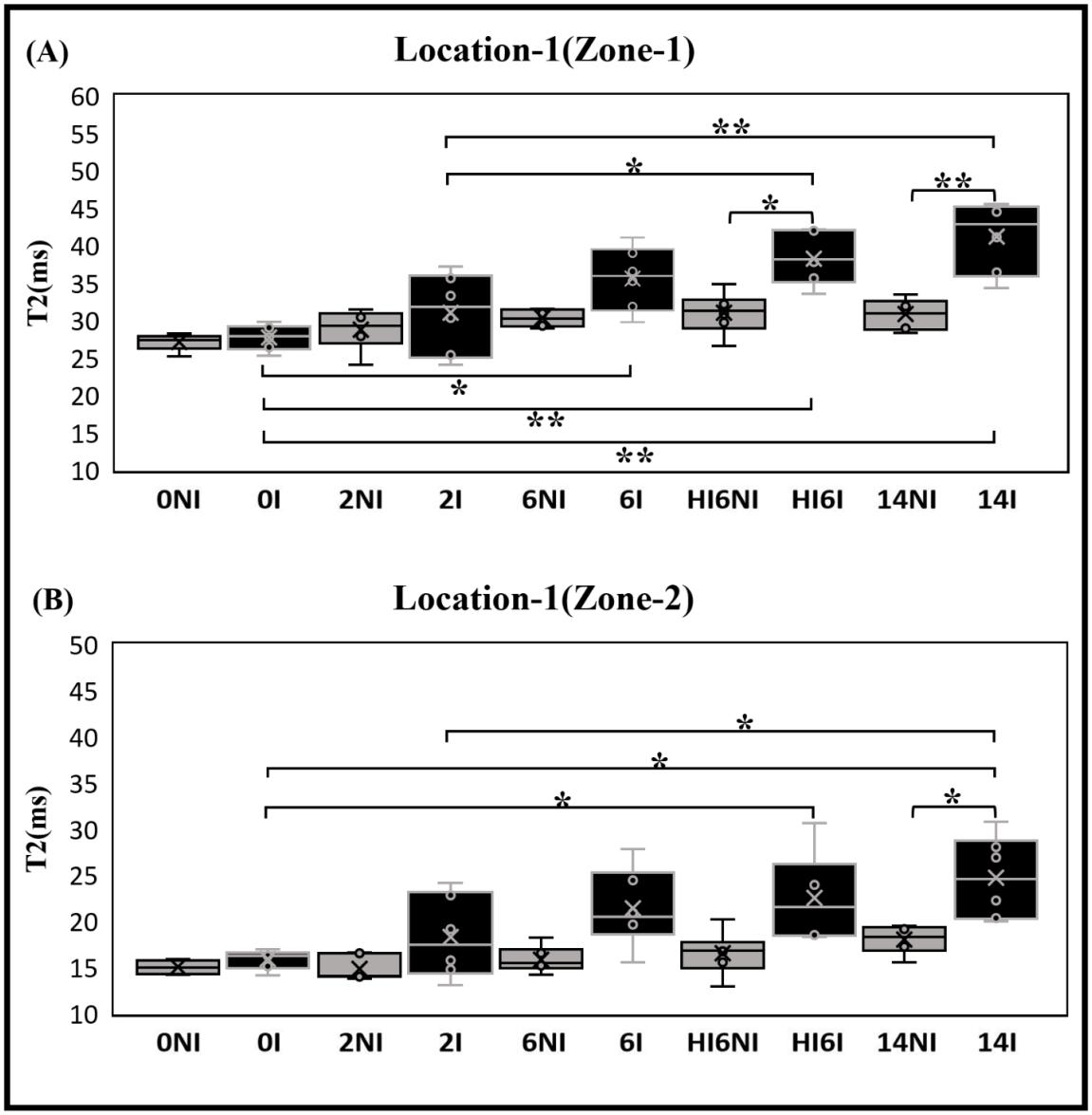

Figure 5.2 Box plots comparing T2 values from the impact location (Location-1) in knee samples. **(A)** Zone-1 represents the upper half of the cartilage, while **(B)** Zone-2 shows the lower half. Data are presented for both non-impact and impact samples at various time points: 0, 2, 6, 6HI, and 14 weeks post-impact. The statistical significances are denoted as *($p < 0.05$) and **($p < 0.0001$).

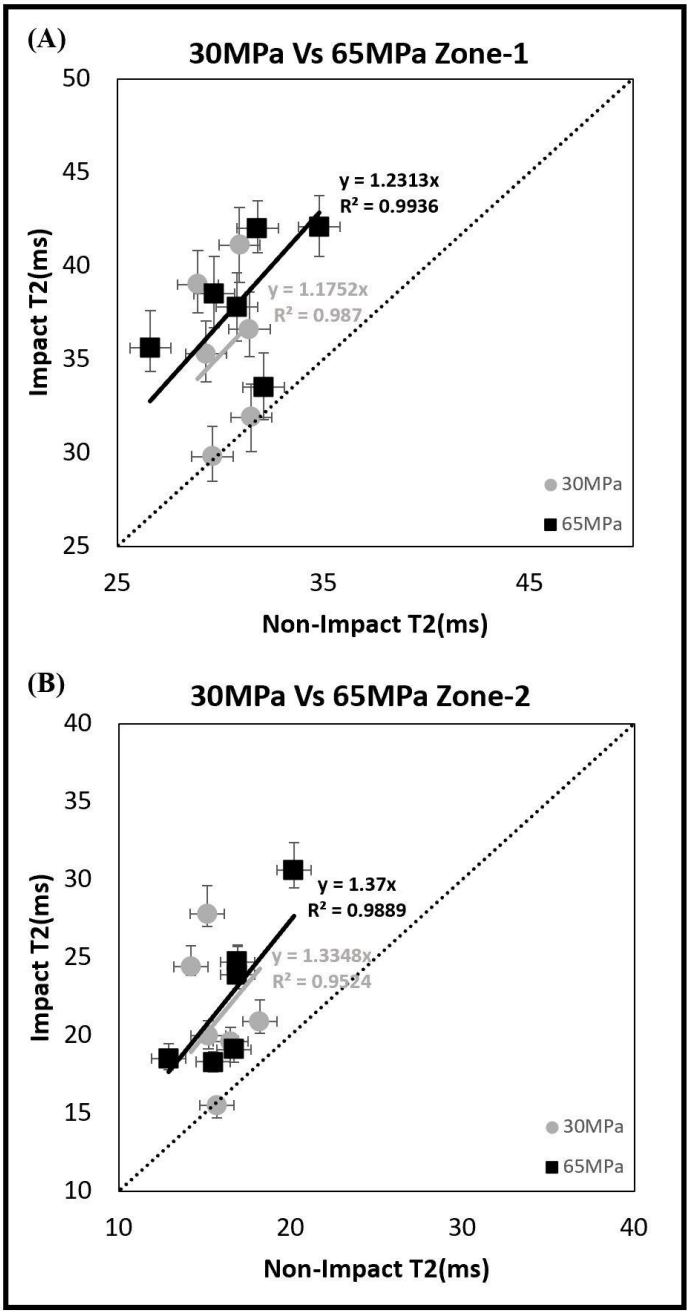

Figure 5.3 Correlation plots showing T2 values for non-impact versus impact knee samples at 6 weeks post-impact, comparing 30MPa and 65MPa impact forces. **(A)** Zone-1 represents the upper half of the cartilage, while **(B)** Zone-2 shows the lower half. The short lines over different data groups are the linearly fitted slope lines. The dotted diagonal line in the center has a slope of one, meaning no change in T2 after impact. Sloped lines above the diagonal denote increment in T2 after impact.

	0-Week (30MPa)	2-Week (30MPa)	6-Week (30MPa)	6-Week (65MPa)	14-Week (30MPa)
Location1:Zone1 T2(ms) Imp	27.72±1.65	30.97±5.3	35.61±4.25	38.25±3.42	41.15±4.8
Location 1:Zone1 T2(ms) Non-Imp	27.06±1.07	28.77±2.7	30.27±1.13	30.97±2.73	30.78±2.04
Difference T2(ms)	+0.66	+2.2	+5.34	+7.28	+10.37
P-Value	1	1	0.29	**0.014**	**< .0001**
Location 1:Zone2 T2(ms) Imp	15.85±1.04	18.25±4.49	21.36±4.25	22.51±4.84	24.7±4.48
Location 1:Zone2 T2(ms) Non-Imp	15±0.73	14.82±1.34	15.82±1.38	16.52±2.36	18.1±1.58
Difference T2(ms)	+0.85	+3.43	+5.54	+5.99	+6.6
P-Value	1	1	0.14	0.066	**0.0204**
Location 2:Zone1 T2(ms) Imp	26.88±2.36	28.7±2.39	29.65±0.71	29.55±2.32	29.22±1.53
Location 2:Zone1 T2(ms) Non-Imp	27.96±2.16	29.13±0.79	28.83±1.75	28.9±2.1	28.21±1.44
Difference	-1.08	-0.43	+0.82	+0.65	+1.01
P-Value	1	1	1	1	1
Location 2:Zone2 T2(ms) Imp	20.23±1.7	20.45±1.48	21.7±2.68	21±2.21	22.91±1.56
Location 2:Zone2 T2(ms) Non-Imp	19.18±1.8	20.76±0.93	20.46±2.32	19.66±1.08	21.51±2.2
Difference	+1.05	-0.31	+1.24	+1.34	+1.4
P-Value	1	1	1	1	1
BMD(g/cm3) Imp	0.72±0.03	0.71±0.01	0.73±0.02	0.71±0.06	0.71±0.03
BMD(g/cm3) Non-Imp	0.71±0.03	0.7±0.03	0.74±0.05	0.72±0.06	0.74±0.06
Difference	+0.01	+0.01	-0.01	-0.01	-0.03
P-Value	1	1	1	1	1

Table 5.1 Summaries of the T2 values from μMRI and BMD measurements from μCT for non-impact and impact samples at different time points: 0, 2, 6, 6HI, and 14 weeks post-impact. The data are presented as mean ± standard deviation along with statistical p-values from the one-way ANOVA with Bonferroni post-hoc test, the bold values in the table represent statistical significance (p-value <0.05).

CHAPTER SIX

ASSESSMENT OF ARTICULAR CARTILAGE DEGRADATION IN RESPONSE TO AN IMPACT INJURY USING μMRI

6.1 Introduction

The excellent load-bearing ability of articular cartilage (AC) can be damaged by the breakdown of the collagen network, loss of GAG, and disruption of the macromolecule-water interactions [92-94]. Many studies in the literature have used microscopic magnetic resonance imaging (μMRI) to study cartilage health [63, 84, 95]. In these MRI studies, T2 relaxation at different orientations of the cartilage specimen with respect to the main magnetic field B_0 is used to non-invasively sub-divide the AC into different zones based on the depth-dependent collagen structures and dipolar interactions among water molecules. These divisions have been consistent with zonal divisions done using polarized light microscopy [61, 63]. The clinical MRI of human cartilage in knees and hips can obtain a transverse resolution of about 0.4-0.6mm/pixel, which is insufficient to study cartilage health in detail. μMRI is the high-resolution version of MRI, which shares the same physics principles and engineering architecture. This identicalness gives μMRI of animal models a direct translational pathway to the clinical MRI investigation in human patients [77, 96]. In the second phase of this project, high-resolution μMRI was used to observe zonal transformations in articular cartilage following knee injury by studying the structural alterations in the superficial zone, transitional zone, and radial zone.

6.2 Results

6.2.1 Morphological Observations

Visual observation of the knee joints was done before the harvesting of the cartilage-bone blocks; all non-impact femoral condyles in the 2 and 14-week groups appeared healthy and had homogeneous coloration throughout the cartilage surface. The impact joints after a 2-week time point showed no visible cartilage deterioration. The impact joints after 14 weeks exhibited slight color change and some of the 14-week impact specimens exhibited deteriorated rough surfaces. Figure 6.1 shows a set of μMRI intensity images at both 0° and 55° orientations along with their respective T2 maps for both 2 and 14-week non-impact and impact specimens. Visually, all non-impact specimens at both 2 and 14 weeks looked normal with a smooth surface. The μMRI intensity images for impact samples at 2 weeks appeared similar to the non-impact samples with no visible damage to the articular surface. The impact specimens at 14 weeks appeared to have damage to the superficial zone as seen in Figure 6.1C, which can be identified by the visual fibrillations at the surface.

6.2.2 Quantitative Analysis

A depth-dependent T2 profile, which had a transverse resolution of 11.7 μm/pixel, was generated from each quantitative T2 image. Applying the zonal division criteria to all T2 profiles, a quantitative analysis of cartilage's T2 characteristics was performed for all specimens. This type of zonal analysis allows for a better sensitivity to detect region-based cartilage degradation for any animal model at a particular degradation time point. Table 6.1 summarizes the analysis of zonal T2 measurements.

First, all zonal T2 results for the 14-week group showed statistically significant rises in T2 values at both 0° and 55° orientations for the impact tissues, when comparing the non-impact and impact specimens. Among the increases, the greatest difference between T2 values for the non-impact and impact comparisons at 14 weeks was found in the superficial tissue and deep tissue. The superficial zone showed a significant 32% increase in T2, while the deep zone exhibited a 30% increase, both indicating notable tissue degradation in the diseased cartilage. For the 2-week group, the differences between the non-impact and impact tissue were mixed, where most tissues in the T2 55° measurements had statistically insignificant differences for the non-impact and impact comparisons, which suggests small/little changes in the impact tissue. These zonal comparisons at 55° are shown graphically in Figure 6.2.

Second, the H_2O% and GAG contents were measured from the adjacent cartilage by the ICP analysis, also summarized in Table 6.1. When compared with the non-impact samples, the water content in the impact samples was higher for both 2 and 14-week groups, although both increases were statistically non-significant. The GAG content in the impact specimens was observed to be lower in both 2 and 14-week groups. The trends shown in these biochemical measurements are mutually consistent and correlative with the μMRI measurements.

Third, the total tissue thickness for both the 2 and 14-week groups, shown in Table 6.1, showed an increase in the impact specimen when compared to the non-impact specimen, by as much as 8% thicker for the 2-week group and 16% thicker for the 14-week group. Although both are statistically non-significant, the trends of these variations mutually support the other measurements.

Finally, the data has three conclusions: (1) There were significant increases in zonal T2 values in the 14-week group impact cartilage when compared with non-impact cartilage; (2) the zonal T2 at 55° can detect T2 changes in all zones while the zonal T2 at 0° can only detect T2 changes in the surface tissue (SZ and TZ), due to the strong dipolar influence on T2 measurement; (3) the biochemical and morphological measurements also support the T2 conclusions.

The data points in the correlation plots in Figure 6.3 were fitted with a linear function. In these plots, the diagonal line in the center has a slope of 1, which means no changes between the comparisons. This technique is visually helpful since all increases will be presented above the diagonal line and all decreases will be presented below the diagonal line. The slopes of all fitted lines with their R^2 values are summarized in Table 6.2. For all tissue zones at both 0° and 55°, the slopes of the linear fits for 14-week specimens were greater than the 2-week slopes, and the slopes of the linear fit for 14-week samples were greater than 1 in all the zones at both 0° and 55°, indicating a substantial increase in the T2 values from the impact after 14 weeks.

6.3 Discussion

Depending on the causes of cartilage degradation several unique alterations may take place in the cartilage tissue [96]. Previous studies indicate that at the early stages of OA, a lesioned cartilage could have higher water content with more water mobility in the AC, decreased GAG content, and an anisotropically altered collagen network; all of which can cause the AC to be swollen (thicker tissue) [60, 97-99]. An OA model in guinea pigs observed a rise in AC thickness for the first 24 weeks, followed by a reduction for the next 28 weeks [100]. Impact on the tissue can cause swelling due to

collagen rupture and rapid GAG loss [101], reduction of GAG in the impact tissues was confirmed by the ICP analysis.

In this study, the water content in the impact specimens was found to increase in the 2 and 14-week groups; at the same time, the GAG content in the impact specimens decreased in the 2 and 14-week groups. These measurements indicate the early structural deterioration in cartilage. Although most of these changes are not statistically significant, the trends in these biochemical measurements between the non-impact and impact samples suggest a biologically meaningful pattern. It is important to highlight that a direct comparison of T2 and GAG data was not feasible. MRI T2 measurement is sensitive to the modification of the molecular mobilities of water molecules in the tissue, which senses the overall molecular interactions that are not the consequence of a single component change. In addition to GAG content, additional structural changes such as tissue hydration, inflammation, collagen structure, and cellular activities might affect the assessment of T2 relaxation time. In contrast, GAG measurement from ICP analysis gives a direct assessment of a bulk measure of GAG content in the tissue. The decrease in GAG content and rise in T2 values in the impact samples both indicate potential degradation and alterations in the tissue microstructure.

The results of this study provide insight into how the illness develops following an initial subcritical mechanical impact. While T2 values in the 2-week impact samples marginally increased in the deeper zones, which may signal the initiation of OA development, the 2-week specimens did not exhibit any visual changes. The worsening of the disease in the AC was observed at 14 weeks, where visual degradation with minor fibrillation in the SZ was noticed in μMRI images. In addition, a significant increase in

zonal T2 values was detected for the 14-week impact specimens and each rabbit's impact knee at 14 weeks had a higher T2 value when compared to its corresponding non-impact knee.

When the cartilage is placed at 55° (magic angle) in the magnet, T2 is least affected by the dipolar interactions and gives better SNR at deeper zones. T2-55° was used to study the effects of OA degradation in the RZ [102]. A significant rise in T2 values in all the cartilage zones of impact specimens at the 14-week time point suggested degradation throughout the tissue, and the highest increase in T2 values was seen in the SZ and RZ2. With the start of PTOA, AC is known to exhibit early degenerative changes in the SZ [86, 103, 104], which is more susceptible to degeneration following a direct impact on the femur condyle due to its location. Higher T2 values in the RZ2 could be related to the damage induced by the impact injury on the calcified cartilage and subchondral bone, disrupting the mineralization structure. Any damage to the subchondral bone can greatly affect the health of the AC [105, 106]. Additional research on the deep region through technologies like microscopic computed tomography (μCT) and polarized light microscopy (PLM) may help in determining the mineralization changes in calcified cartilage and the subchondral bone plate.

In Figure 6.3, correlation plots for T2-55° showed higher T2 linear fit slope trends in all the zones for 14-week specimens compared to the 2-week specimens, suggesting the condition worsened with time. Significantly higher T2 levels at 14 weeks in the impact tissue indicated changes in the ECM composition and hydration levels of the AC. Extending the monitoring duration beyond 14 weeks in future studies can prove helpful to better understand the long-term consequences of impact damage on the AC.

6.3.1 Conclusions

In this study, μMRI at high resolution successfully detected zonal deterioration in the femoral articular cartilage at 14 weeks following a single subcritical injury. The μMRI data from this study characterized higher T2 values as a function of PTOA progression and confirmed a positive correlation between tissue degradation and T2 values. The ICP analysis in this study also supported the relationship between increased T2 values and cartilage deterioration. Although the pathological features of PTOA progression in animal models differ from human PTOA, this study has the potential to improve future diagnostic methods for the early detection and management of human PTOA. This study has been published in Connective Tissue Research [88].

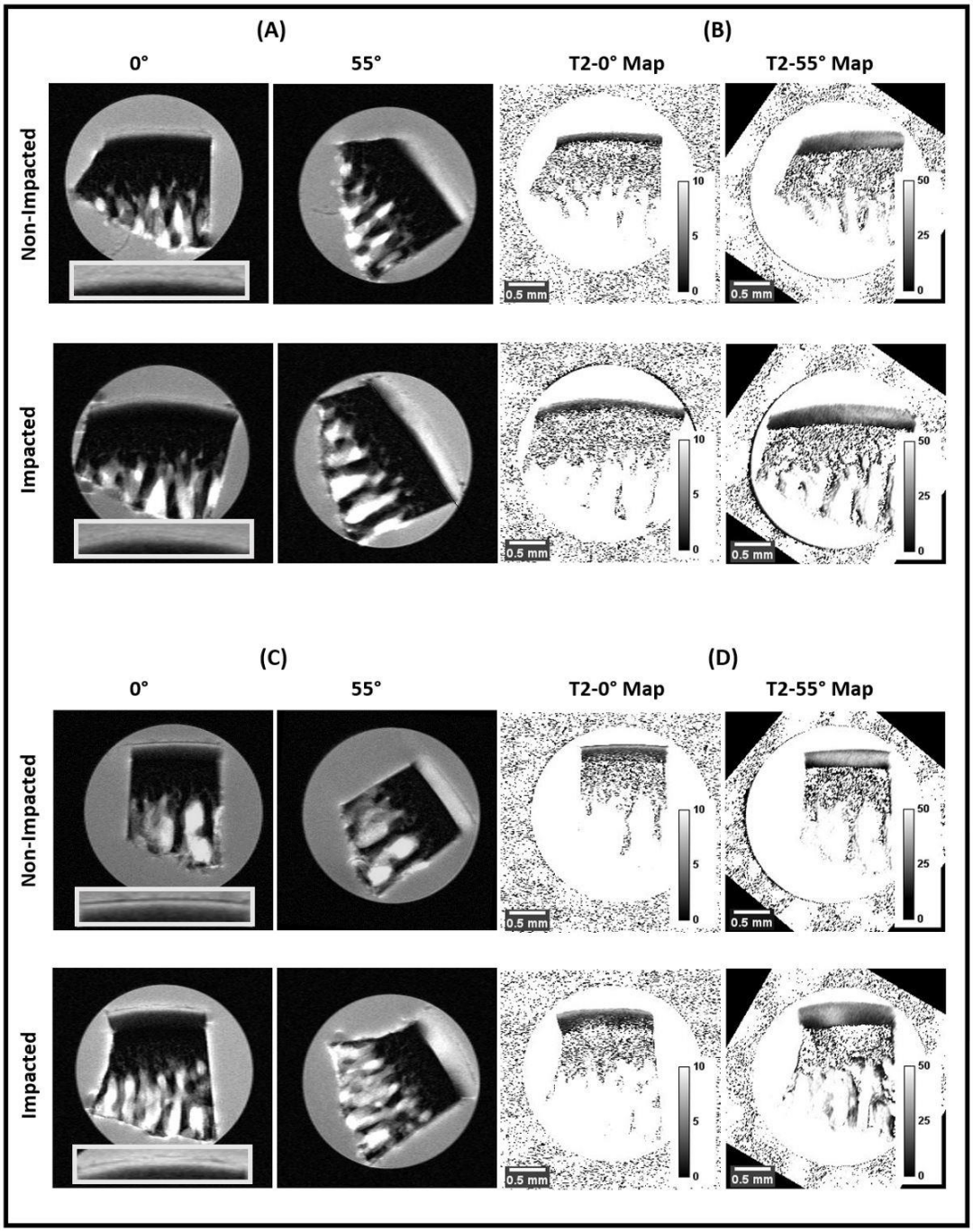

Figure 6.1 Representative set of the quantitative μMRI T2-weighted intensity images **(A, C)** and T2 maps **(B, D)** at 0° and 55°, zoomed-in articular surface is shown at the bottom of 0° intensity images. **(A-B)** are from the 2-week group; **(C-D)** are from the 14-week group.

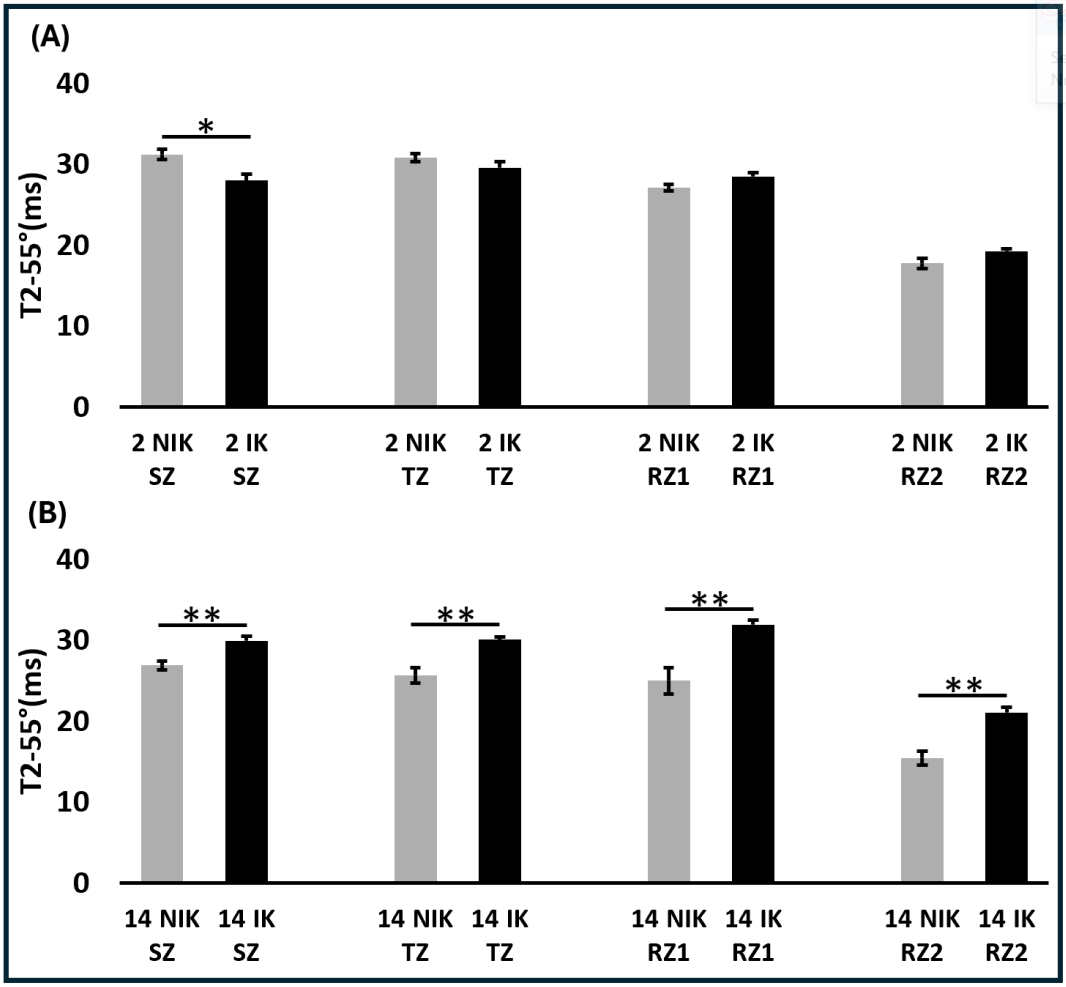

Figure 6.2 Bar graphs comparing T2 values between non-impact knees (NIK) and impact knees (IK) at **(A)** 2 weeks and **(B)** 14 weeks, based on zonal data from the Superficial Zone (SZ), Transitional Zone (TZ), Radial Zone 1 (RZ1), and Radial Zone 2 (RZ2). The statistical significances are denoted as *($p < 0.05$) and **($p < 0.0001$).

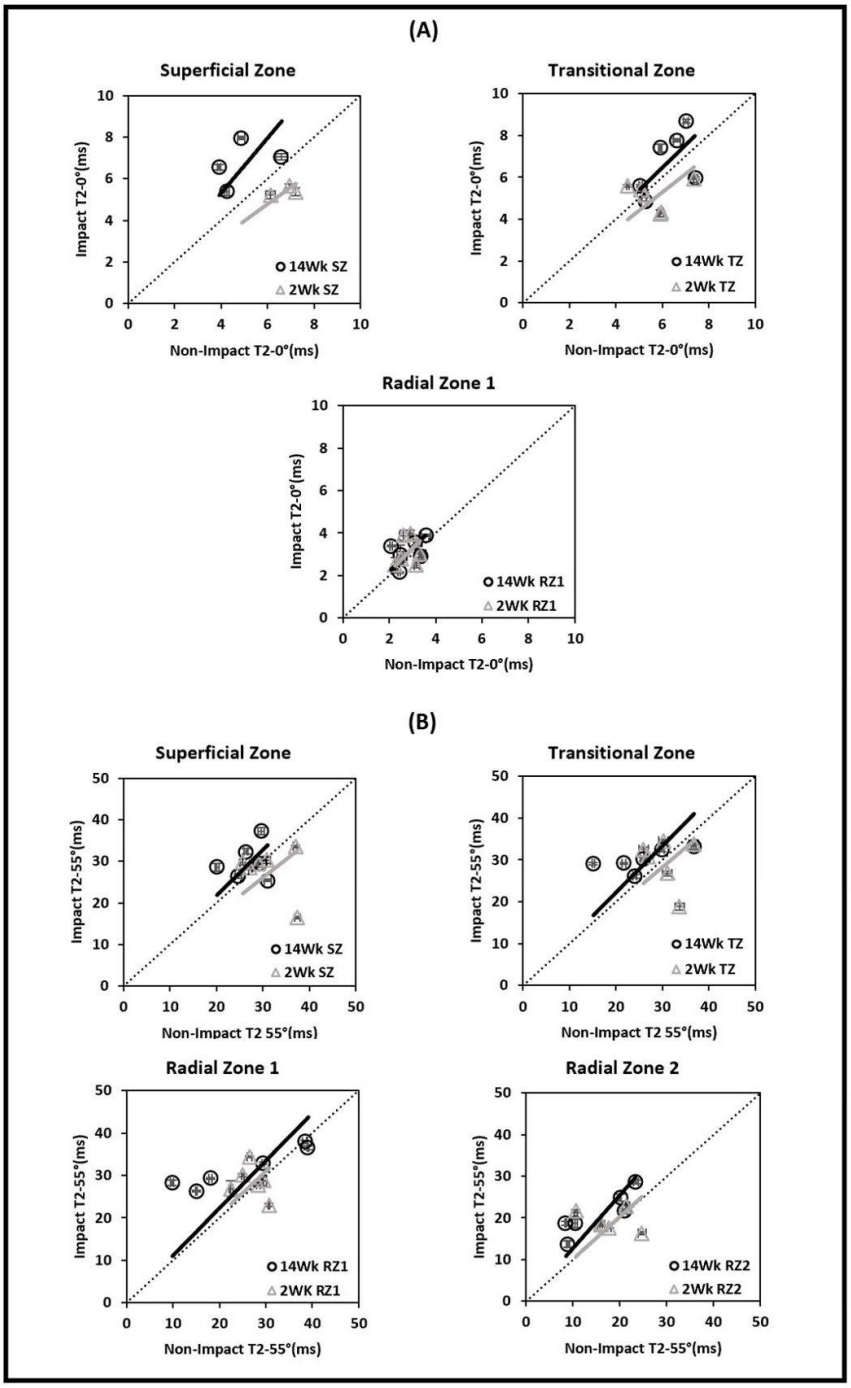

Figure 6.3 Correlation plots between the zonal T2 values of the non-impact vs impact specimens for both the 2-week and 14-week groups, (A) T2 at 0°, and (B) T2 at 55°. The short lines over different data groups are the linearly fitted slope lines. The dotted diagonal line in the center has a slope of 1, meaning no change in T2 after impact. Slope lines above the diagonal mean increment in T2 after impact, and below the diagonal mean decrement.

	2-Week NIK Vs 2-Week IK			14-Week NIK Vs 14-Week IK		
	2-Week NIK	**2-Week IK**	**% Diff.**	**14-Week NIK**	**14-Week IK**	**% Diff.**
T2-0° SZ (ms)	6.29 ±0.17	5.77 ±0.16	- 8.6%	4.92 ±0.15	6.86 ±0.14	**+ 32.9%**
T2-0° TZ (ms)	5.67 ±0.13	5.11 ±0.09	**- 10.3%**	6.22 ±0.12	6.75 ±0.18	**+ 8.1%**
T2-0° RZ1 (ms)	2.80 ±0.08	3.10 ±0.12	**+ 10.1%**	2.84 ±0.08	3.27 ±0.11	**+ 14.0%**
T2-55° SZ (ms)	31.19 ±0.63	27.98 ±0.74	**- 10.8%**	26.86 ±0.53	29.91 ±0.58	**+ 10.7%**
T2-55° TZ (ms)	30.78 ±0.51	29.53 ±0.74	- 4.1%	25.62 ±0.89	30.04 ±0.36	**+ 15.8%**
T2-55° RZ1 (ms)	27.07 ±0.41	28.47 ±0.58	+ 5.0%	24.97 ±1.48	31.87 ±0.58	**+ 24.2%**
T2-55° RZ2 (ms)	17.75 ±0.62	19.24 ±0.35	+ 8.0%	15.41 ±0.83	21.03 ±0.68	**+ 30.8%**
H_2O %	74.19 ±2.10	81.54 ±3.37	+ 9.4%	72.52 ±2.82	78.82 ±1.36	+ 8.3%
GAG (mg/ml)	71.39 ±8.18	54.79 ±5.56	- 26.3%	71.16 ±6.01	55.74 ±5.15	- 24.3%
Thickness (µm)	208.65 ±8.23	228.15 ±5.01	+ 8.9%	222.30 ±27.19	263.25 ±32.08	+ 16.8%

Table 6.1 Summary of the µMRI and ICP measurements, including T2 (ms), H2O (%), GAG (mg/ml), and tissue thickness (µm). The data is presented as the mean ± standard errors. Percentage differences are listed in the table, with bold values indicating statistical significance ($p < 0.05$).

Tissue Zone	T2-0° Impact Vs Non-Impact Femur			
	2-Week		14 Week	
	Slope	R^2 Value	Slope	R^2 Value
SZ	0.80	0.99	1.33	0.96
TZ	0.88	0.96	1.02	0.97
RZ1	1.09	0.95	1.09	0.96
RZ2				
Tissue Zone	T2-55° Impact Vs Non-Impact Femur			
	2-Week		14 Week	
	Slope	R^2 Value	Slope	R^2 Value
SZ	0.87	0.92	1.10	0.97
TZ	0.94	0.94	1.11	0.96
RZ1	1.04	0.97	1.12	0.91
RZ2	1.01	0.91	1.27	0.96

Table 6.2 Summary of the slopes and the R^2 values of the fitted lines in the zonal T2 correlation plots.

CHAPTER SEVEN

HIGH-RESOLUTION ASSESSMENT OF POST-TRAUMATIC MICROSTRUCTURAL ALTERATIONS IN THE RABBIT KNEE CARTILAGE AND SUBCHONDRAL BONE

7.1 Introduction

In articular cartilage [61, 107], the superficial zone (SZ), transitional zone (TZ), and radial zone (RZ) are part of the uncalcified tissue, while the calcified zone (CZ) is located in the deepest region of the AC bounded by the tidemark and the cement line bordering the subchondral bone [102]. Mineralization in the CZ provides a gradual transition of mechanical properties from the soft cartilage to the hard subchondral bone. This transition is crucial for joint stability and functionality [108, 109]. Calcium content is the major component in the CZ, accounting for 65-75% of the dry weight [110]. Just beneath the CZ lies the subchondral bone, a vital structure that supports the AC and helps in the even and gradual distribution of the mechanical load. The subchondral bone is anatomically divided into two structures: subchondral bone plate (SBP) and subchondral trabecular bone (STB) [111]. SBP is a thin layer located directly under the CZ consisting of tiny channels containing blood vessels and nerves that link the STB and the CZ, the size and number of these channels can change with age, pressure, and injuries [112, 113]. Relative to SBP, STB is more porous and consists of blood vessels, sensory nerves, and bone marrow. STB demonstrates a strong structural anisotropy [67, 114].

Remodeling and mineralization changes in the CZ and SBP during the progression of post-traumatic osteoarthritis (PTOA) can affect the mechanical and biological stability of the joint. In the third phase of this project, we used advanced high-

resolution imaging techniques including polarized light microscopy (PLM), microscopic computed tomography (μCT), and inductively coupled plasma (ICP) to analyze early-stage cartilage and subchondral bone deterioration after a mechanical injury, aiming to develop better diagnostic methods for OA.

7.2 Results

7.2.1 PLM and ICP Analysis

Before the specimens were harvested, the knee joints were visually inspected. All non-impact femoral condyles in the 2- and 14-week specimens looked healthy and had uniform coloring across the cartilage surface. For the 2-week impact joints, there was no significant visual cartilage degeneration. For the 14-week impact joints, a few impact joints showed slight discoloration in the area of impact.

Figure 4.2 shows representative quantitative optical retardation images of non-impact (A) and impact (B) cartilage samples at a high resolution of 1.0 μm/pixel, followed by their respective depth-dependent profiles. All individual data points from all optical retardation depth-dependent profiles (i.e., all specimens) were pooled and compared in Figure 7.1, between the non-impact and impact samples at the 2-week and 14-week periods. In Figure 7.1, the depth-dependent data points of quantitative optical retardation values in cartilage were divided into four zones, to examine the effects of the impact on cartilage at various depths. The diagonal line in the correlation plots has a slope of 1, which indicates no change between the comparisons. Any increase in the comparison will be displayed by shift in data points above the diagonal line and any decrease will be displayed below the diagonal line. The average value of each zone for non-impact and impact samples at 2 and 14 weeks is shown in Table 7.1.

Figure 7.1 shows that the comparisons between non-impact and impact samples at 2 weeks had no major shifts between the two groups since data points were approximately equally spread out across the diagonal for all four regions. In contrast, the comparison between non-impact and impact samples at 14 weeks displayed skewed data points for two regions. Both the SZ and the CZ had skewed data points below the diagonal line, illustrating a reduction in the optical retardation measurements for the impact group. Most shift in the optical retardation values was observed for the CZ where most of the data points were below the diagonal line, shift in the CZ region was statistically significant. The relevant region for CZ is highlighted with an ellipse-shaped boundary in the figure.

Figure 7.2 shows the depth-dependent optical retardation profiles averaged from all specimens, for both non-impact and impact groups at the 2-week and 14-week periods. At the 2-week time point, the depth-dependent profiles between the non-impact and the impact groups were almost similar. In contrast, at the 14-week time point, the depth-dependent profile for the impact group had lower values in SZ and CZ, with the CZ having the largest differences (both trends are reflected in the spreading of the individual data points in Figure 7.1). While the zonal optical retardation values between the non-impact and impact specimens showed no prominent differences at 2 weeks. At 14 weeks, the SZ showed a reduction of 22% in retardation values in the impact group, while the TZ and the RZ showed a minor drop of 0.9% and 6% respectively for impact samples. The CZ at 14 weeks showed a 29% decrease in retardation values in the impact group, this decrease was statistically significant (p-value <0.05). These changes in the optical retardation values are displayed using the box plots in Figure 7.3.

Table 7.1 also summarizes the calcium concentration in the cartilage specimens measured by ICP analysis (calcium content is largely contributed from the CZ of the cartilage). When comparing the non-impact and impact groups at 2 weeks, the calcium concentration in the impact group compared to the non-impact group showed no significant changes. The comparison at 14 weeks displayed an average drop of 0.211 mM in the impact group compared to the non-impact group, this difference between the two groups was statistically significant (p-value <0.05). This analysis was helpful to support the changes observed in the CZ optical retardation values for the impact group as well as the findings in the 14-week BMD measurements from μCT.

7.2.2 μCT Analysis on the Subchondral Bone

To investigate the changes in the mineralization in the SBP initiated by the impact event, we carried out BMD analysis on the cartilage-bone blocks using μCT imaging at a high resolution of 6.7 μm. The change in the SBP's BMD was found to be statistically insignificant for the non-impact Vs impact groups at 2 weeks, with a decrease of 0.1% in the impact group. In comparison, at 14 weeks the BMD dropped in the impact group with a change of 6.3%, which was statistically significant (p-value <0.05). These changes in the BMD are displayed using the box plots in Figure 7.4B.

The SBP was evenly divided into two regions, from which the BMD values were measured, as shown in Figure 7.4A. Box plots in Figure 7.4C for non-impact and impact groups with BMD measurements were created for the two regions of SBP. It can be seen that the 2-week specimens in both regions showed very little changes in the BMD measurements between the non-impact and impact groups. The 14-week specimens for

both regions showed higher deviation compared to the 2-week specimens, both regions noted a drop in BMD values for the impact group.

7.3 Discussion

The high-resolution PLM and μCT examination aimed to track the micro-structural changes in the AC and the SBP by quantitatively analyzing the optical retardation and BMD changes in the specimens. The intention of our subcritical impact [91] was not to cause extensive or penetrative damage to the cartilage-bone specimen. We aimed to find out if the early changes in the impact specimens could be successfully identified. The assessment of cartilage-bone block quality can be determined by important factors like microdamage in peri-articular mineralized tissue such as CZ of the cartilage and the SBP [115]. Any early deterioration that is successfully identified may help in the future development of a therapeutic intervention that may stop or reverse tissue degeneration. This project's findings attest to the early PTOA's effective identification.

In this study, quantitative analysis of optical retardation measurements from PLM images displayed notable changes in birefringent properties of the cartilage after an impact injury [116]. At the 14-week post-impact surgery, we observed a significant reduction in optical retardation values of impact samples compared to the non-impact samples, particularly in the CZ. When analyzing the CZ region in Figure 7.1 and Figure 7.3, notable differences emerged where the majority of the retardation values in the CZ from the impact samples showed a prominent decrease. This observation confirmed structural changes in the CZ from the applied impact. However, at 2 weeks post-impact surgery, no significant reduction was observed in the impact cartilage, which confirmed

the nature of our sub-critical impact. While minimal changes were observed at the 2-week mark, changes were more pronounced and evident at 14 weeks, indicating a progressive nature of cartilage degradation over time.

At the 14-week time point, we observed a significant reduction in calcium concentration in the impact samples. The drop in the calcium concentration seen in the ICP analysis aligned with the optical retardation results of the PLM findings. Past studies indicated that early-stage remodeling of CZ and SBP can differ from the later stages of PTOA. In the early stages, CZ and SBP are known to undergo osteopenia, characterized by a decrease in mineral density. Whereas at later stages remodeling of the CZ and SBP can take a different trajectory exhibiting signs of sclerosis during which an increase in mineral density can be observed [65, 117-119]. CZ is the region in the cartilage where the calcium is deposited during the mineralization process. So, a significant reduction in calcium concentration in the cartilage can be indicatively responsible for the altered optical retardation values observed in the CZ of impact samples at 14 weeks.

In a prior μMRI investigation of early-stage PTOA in rabbit knees, structural degradation was noted in the SZ and the deep zone [88, 91]. After a direct hit to the surface of the femur condyle, the SZ was expected to show early degenerative alterations due to its location at the surface of the tissue at the impact point. Also, the SZ is known to show early degenerative alterations with the onset of PTOA [103, 104]. With its high stiffness, CZ has been found to be one of the first zones affected by trauma [120]. CZ is a critical region where mineralization occurs in the cartilage, changes in this zone can have serious implications on cartilage health [117, 121, 122]. Optical retardation changes observed in the CZ in this study strongly indicated alterations in the deposition of

minerals, mainly calcium [110]. Any changes in the mineralization can lead to compromised structure and functionality of the cartilage subsequently. The changes in the mineralization of the CZ can greatly affect the load-bearing ability of the cartilage in diseases like OA [123].

Subchondral bone plays a crucial role in supporting the AC, which is known to undergo structural changes with OA progression [113]. In this study, we aimed to understand how the BMD is affected in the SBP after a single subcritical impact. At 2 weeks no significant differences in BMD were noted between the non-impact and impact specimens. However, at 14 weeks, a statistically significant drop in BMD was observed in the SBP of impact samples. This difference again suggested the progressive structural changes from a subcritical injury in the bone plate over time. The altered BMD in the SBP at 14 weeks could be indicative of the changes in mineralization pattern as a response to the microdamage from the impact. In various animal studies, subchondral bone loss has been reported at the early stages of OA pathogenesis. Also, deterioration of the SBP has been related to cartilage degradation in OA [124-126]. Significant remodeling and subchondral bone loss in human OA have also been observed at early stages [127]. Both halves of the SBP in our study showed changes in the BMD between non-impact and impact samples at 14 weeks. The BMD measurements in SBP from μCT were in line with PLM findings of optical retardation values in the CZ of the cartilage.

7.3.1 Conclusions

In this study, we investigated the effects of a subcritical impact on rabbit knee AC and SBP at 2 and 14 weeks post-impact surgery. With the use of multiple techniques including PLM imaging, μCT imaging, and ICP analysis, we assessed the response of AC

and SBP to a subcritical impact and obtained several significant findings. At 2 weeks the degradation was not prominent, however, at 14 weeks statistically significant changes were evident. PLM imaging analysis exhibited reduced optical retardation values in the CZ of impact AC, indicating early structural changes in cartilage. A decline in calcium concentration was noted for the 14-week impact AC samples, implying mineralization changes in response to the impact. μCT analysis of SBP at 14 weeks showed BMD reduction in the impact samples compared to the non-impact samples. The BMD changes observed in the impact samples suggest bone remodeling in response to the impact. The observed alterations in optical retardation, calcium concentration, and BMD are collectively suggestive of early responses in AC and SBP due to a subcritical injury. The findings of this study have the potential to improve the knowledge about the early-stage progression of injury-related joint degradation, which can be useful in timely diagnosis and intervention for preserving joint health. This study has been published in the Journal of Anatomy [128].

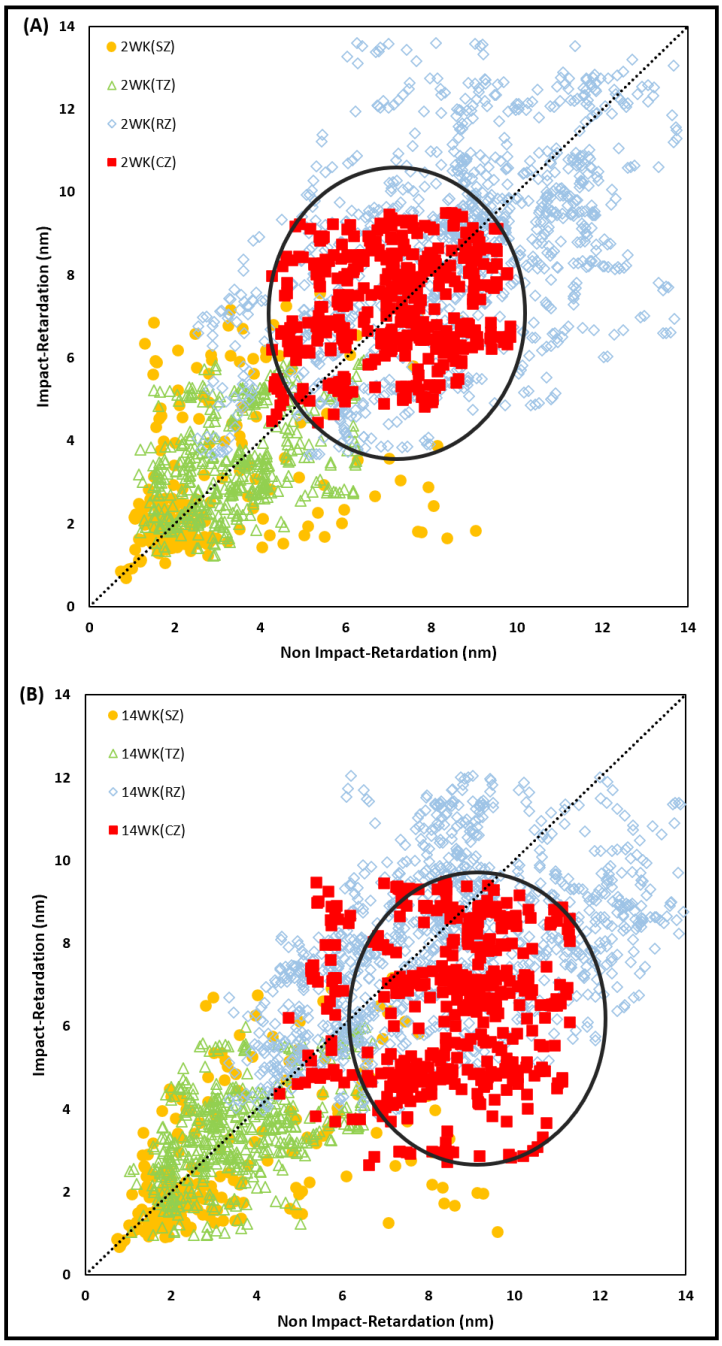

Figure 7.1 Pixel values from depth-dependent optical retardation profiles, correlating the non-impact and impact specimens from **(A)** 2-week group, where no major shifts were noted. Slopes for each zone at 2-Week: SZ-0.83, TZ-0.94, RZ-0.97, and CZ-0.99. **(B)** 14-week group, showing a shift in values in the superficial and the calcified zone. Slopes for each zone at 14-Week: SZ-0.69, TZ-0.89, RZ-0.89, and CZ-0.74. The diagonal dotted line (slope =1) indicates no change. Points above show an increase post-impact and points below show a decrease post-impact.

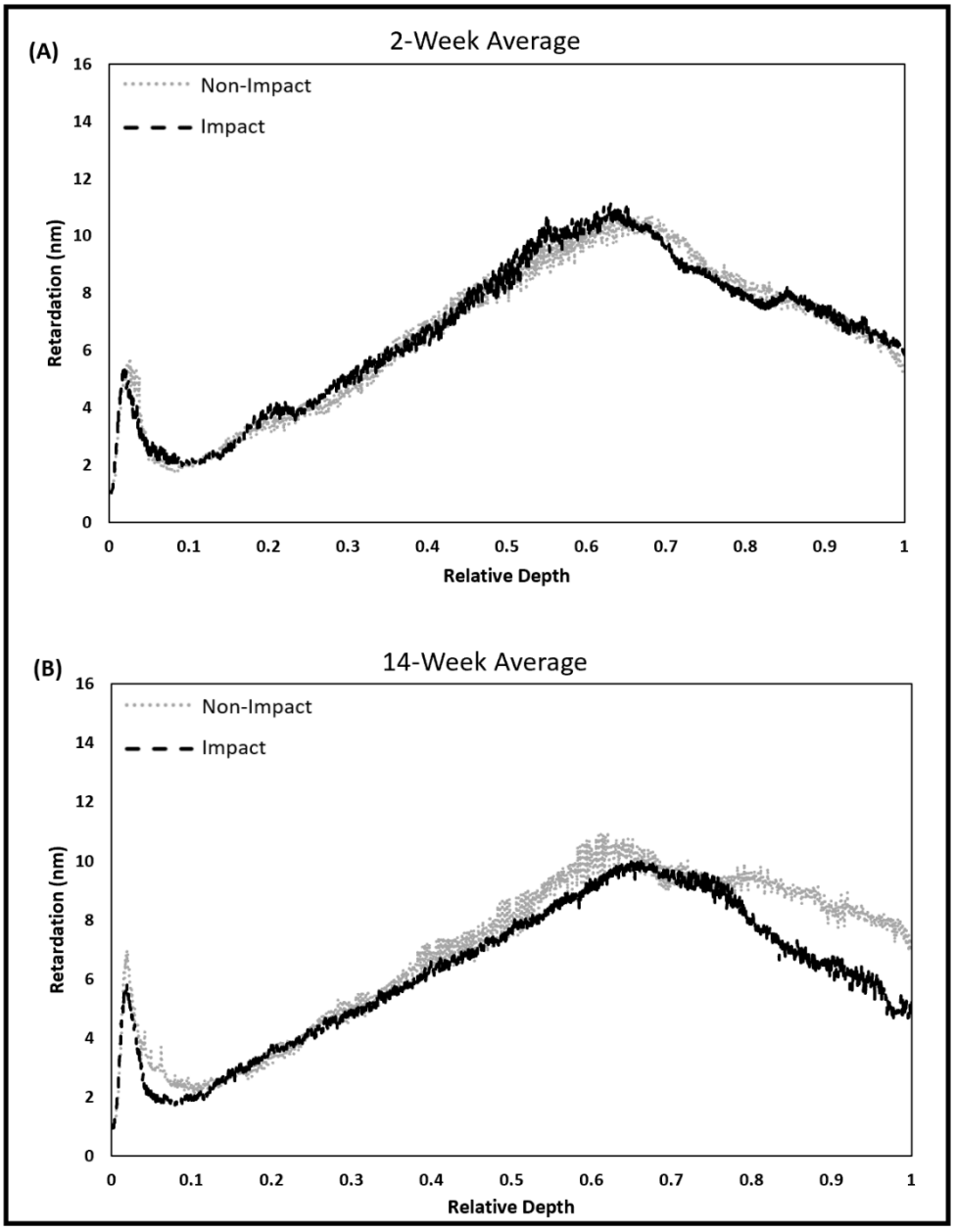

Figure 7.2 Comparison of averaged depth-dependent optical retardation profiles from all samples, between the non-impact vs impact specimens, at **(A)** 2 weeks and **(B)** 14 weeks post-impact. Zonal division of the cartilage: SZ(0-0.1), TZ(0.1-0.3), RZ(0.3-0.8), and CZ(0.8-1.0).

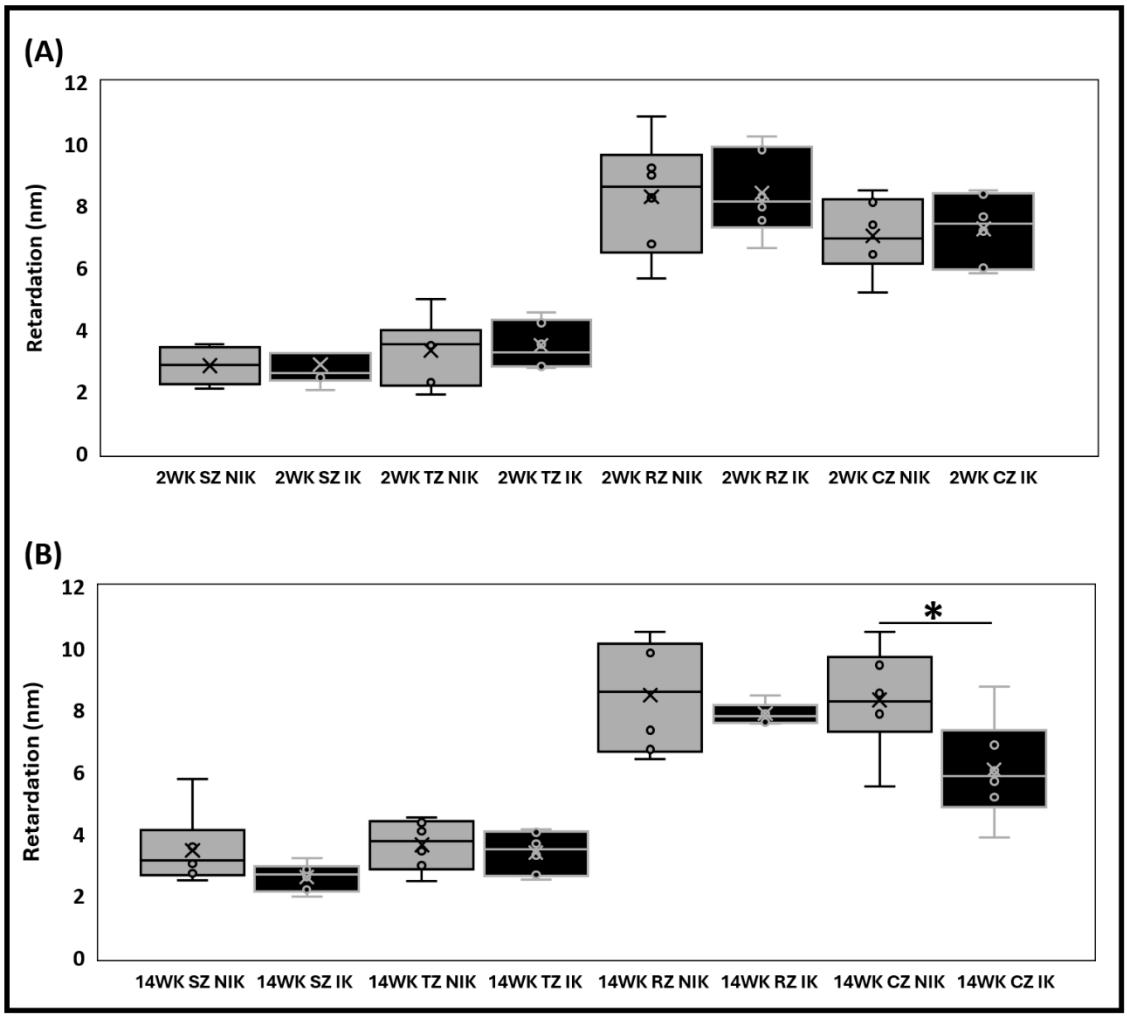

Figure 7.3 Box plots comparing depth-dependent quantitative analysis of optical retardation among non-impact and impact samples at **(A)** 2-week and **(B)** 14-week post-impact. The analysis depicts statistically significant changes at a 14-week comparison in the calcified zone. Statistical significance is denoted as *(p-value <0.05).

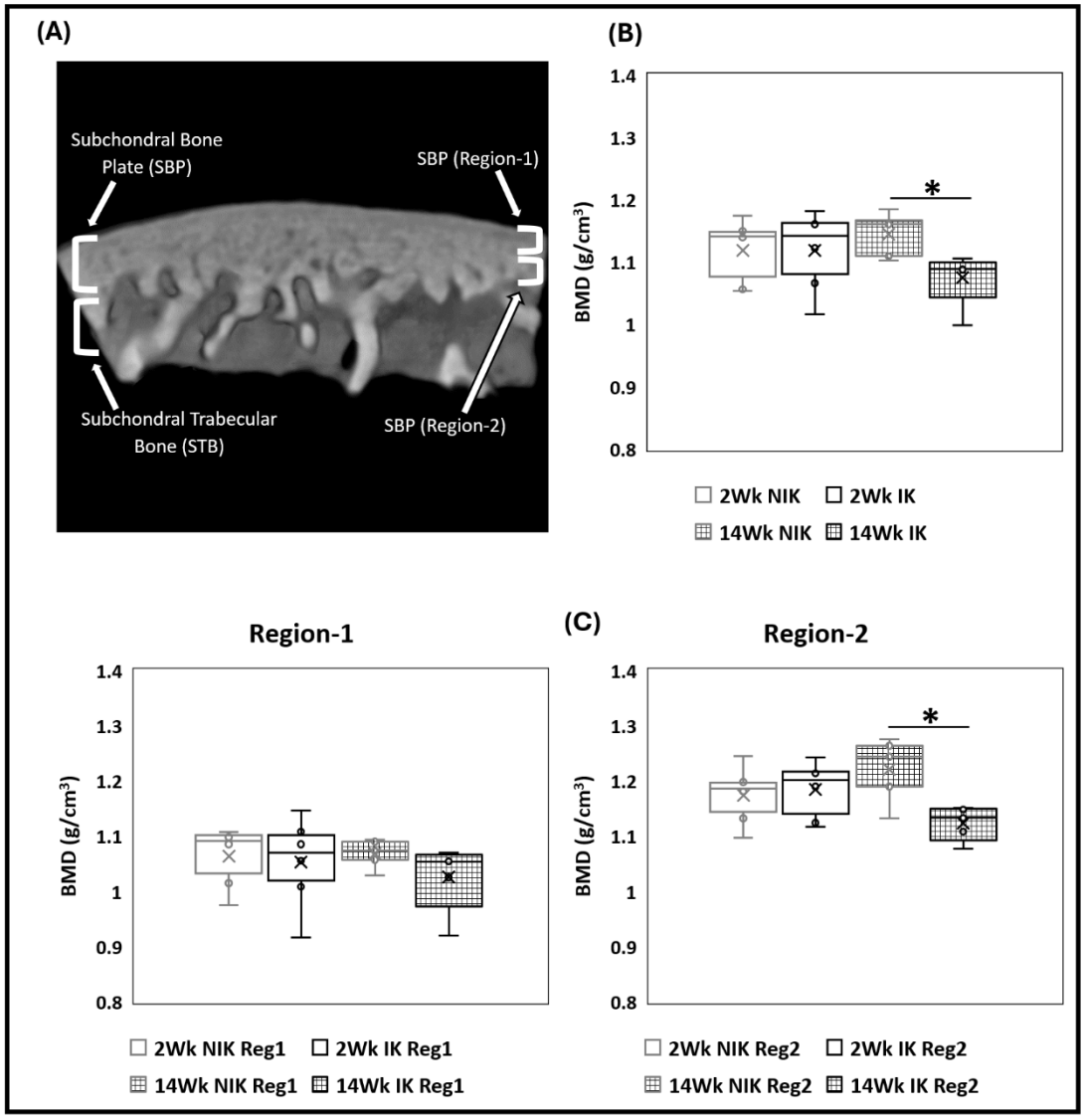

Figure 7.4 (A) 3D representation of rabbit knee subchondral bone using μCT imaging. **(B)** Box plots display bone mineral density (BMD) data from non-impact and impact subchondral bone plate (SBP) samples at 2-week and 14-week post-impact, where the statistical significance is denoted as *(p-value <0.05). The data in these plots was taken from the entire SBP region. **(C)** Box plots display the region-wise BMD data from the non-impact and impact samples at 2 weeks and 14 weeks. The region-1 data was measured from the upper half of the SBP and region-2 data was measured from the lower half of the SBP as shown in **(A)**. Statistical significance is denoted as *(p-value <0.05).

	2-Week NIK Vs 2-Week IK				14-Week NIK Vs 14-Week IK			
	2-Week NIK	**2-Week IK**	**% Diff.**	**P Value**	**14-Week NIK**	**14-Week IK**	**% Diff.**	**P Value**
Ret(nm) SZ	2.83 ±0.11	2.84 ±0.1	+ 0.4%	0.9	3.27 ±0.13	2.63 ±0.09	- 21.7%	0.1
Ret(nm) TZ	3.36 ±0.06	3.52 ±0.05	+ 4.6%	0.7	3.51 ±0.06	3.48 ±0.05	- 0.9%	0.5
Ret(nm) RZ	8.40 ±0.07	8.45 ±0.06	+ 0.6%	0.8	8.36 ±0.07	7.89 ±0.05	- 5.8%	0.4
Ret(nm) CZ	7.17 ±0.06	7.23 ±0.06	+ 0.8%	0.6	8.49 ±0.07	6.35 ±0.08	- 28.8%	**0.01**
Calcium (mM)	0.389 ±0.145	0.297 ±0.158	- 23.6%	0.5	0.455 ±0.102	0.244 ±0.059	-46.3%	**0.02**
BMD(g/cm^3) Avg. SBP	1.119 ±0.022	1.118 ±0.027	- 0.1%	0.9	1.144 ±0.028	1.074 ±0.021	- 6.3%	**0.01**
BMD(g/cm^3) Region-1	1.064 ±0.022	1.053 ±0.033	- 1.0%	0.8	1.068 ±0.011	1.026 ±0.027	- 4.0%	0.2
BMD(g/cm^3) Region-2	1.174 ±0.021	1.184 ±0.021	+ 0.8%	0.6	1.221 ±0.026	1.123 ±0.013	- 8.3%	**0.03**

Table 7.1 Summaries of the optical retardation, calcium content, and BMD measurements. The data are presented as mean ± standard error along with percentage differences and statistical p-values from the Paired Student t-Test, the bold values in the table represent statistical significance (p-value <0.05).

CHAPTER EIGHT

SUMMARY AND FUTURE DIRECTIONS

This dissertation research focused on tracking the progression of post-traumatic osteoarthritis (PTOA) using microscopic imaging techniques, including microscopic magnetic resonance imaging (μMRI), polarized light microscopy (PLM), and microscopic computed tomography (μCT). These high-resolution imaging methods provided details on the structural changes happening in the articular cartilage and subchondral bone during the early stages of PTOA using a rabbit model.

We used quantitative MRI T2 mapping to assess the integrity of femoral articular cartilage non-invasively and non-destructively. This approach successfully detected cartilage degradation through changes in the extracellular matrix (ECM), allowing us to identify the earliest signs of osteoarthritis (OA). PLM in combination with μMRI allowed us to examine the structural changes that occurred in different zones of the articular cartilage in greater detail at optical resolution. The retardation values in PLM imaging enabled us to detect modifications in the collagen network within the cartilage and alterations in mineralization patterns in the calcified zone of the cartilage. The mechanical properties of cartilage become compromised when collagen fibers lose their structural integrity in OA. The analysis of subchondral bone alterations was done through μCT examinations which revealed patterns of BMD changes with the progression of OA. The high-resolution imaging methods helped in the evaluation of knee joint response to a mechanical injury. These multidisciplinary methods offered comprehensive information

about separate features of the disease which provided a more detailed understanding of the changes occurring in the joint at early stages of knee OA.

Identifying early biological signs can help to track the progression of OA accurately. The findings of this dissertation may lead to several possible directions for future research focusing on the diagnosis and treatment of OA in animal models. We could study pharmacological drugs and gene-based regenerative treatments as possible ways to halt cartilage degradation, regenerate cartilage tissue, and enhance joint movement during OA. Gene therapies, drug treatments, and physical therapy could be the focus of future research as the extension of this dissertation study, as they might slow down cartilage breakdown, reduce inflammation, and promote the regeneration of cartilage tissue. Advanced imaging methods such as MRI, CT, and PLM can enable clinicians and researchers to monitor treatment effectiveness and develop optimized treatment plans for OA patients to enhance their quality of life.

APPENDIX A

COPYRIGHT LETTERS OF PERMISSION TO REPRODUCE

Permission to reproduce Figure 2.1

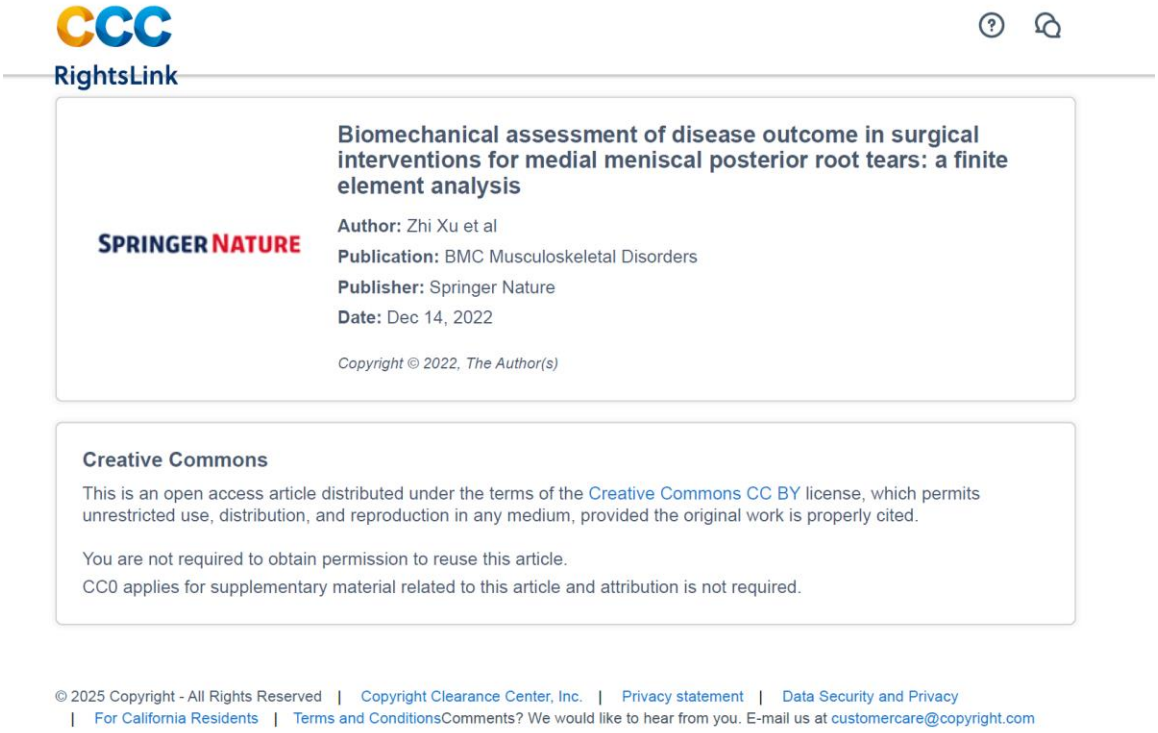

RightsLink

SPRINGER NATURE

Biomechanical assessment of disease outcome in surgical interventions for medial meniscal posterior root tears: a finite element analysis

Author: Zhi Xu et al

Publication: BMC Musculoskeletal Disorders

Publisher: Springer Nature

Date: Dec 14, 2022

Copyright © 2022, The Author(s)

Creative Commons

This is an open access article distributed under the terms of the Creative Commons CC BY license, which permits unrestricted use, distribution, and reproduction in any medium, provided the original work is properly cited.

You are not required to obtain permission to reuse this article.

CC0 applies for supplementary material related to this article and attribution is not required.

Permission to reproduce Figure 2.2

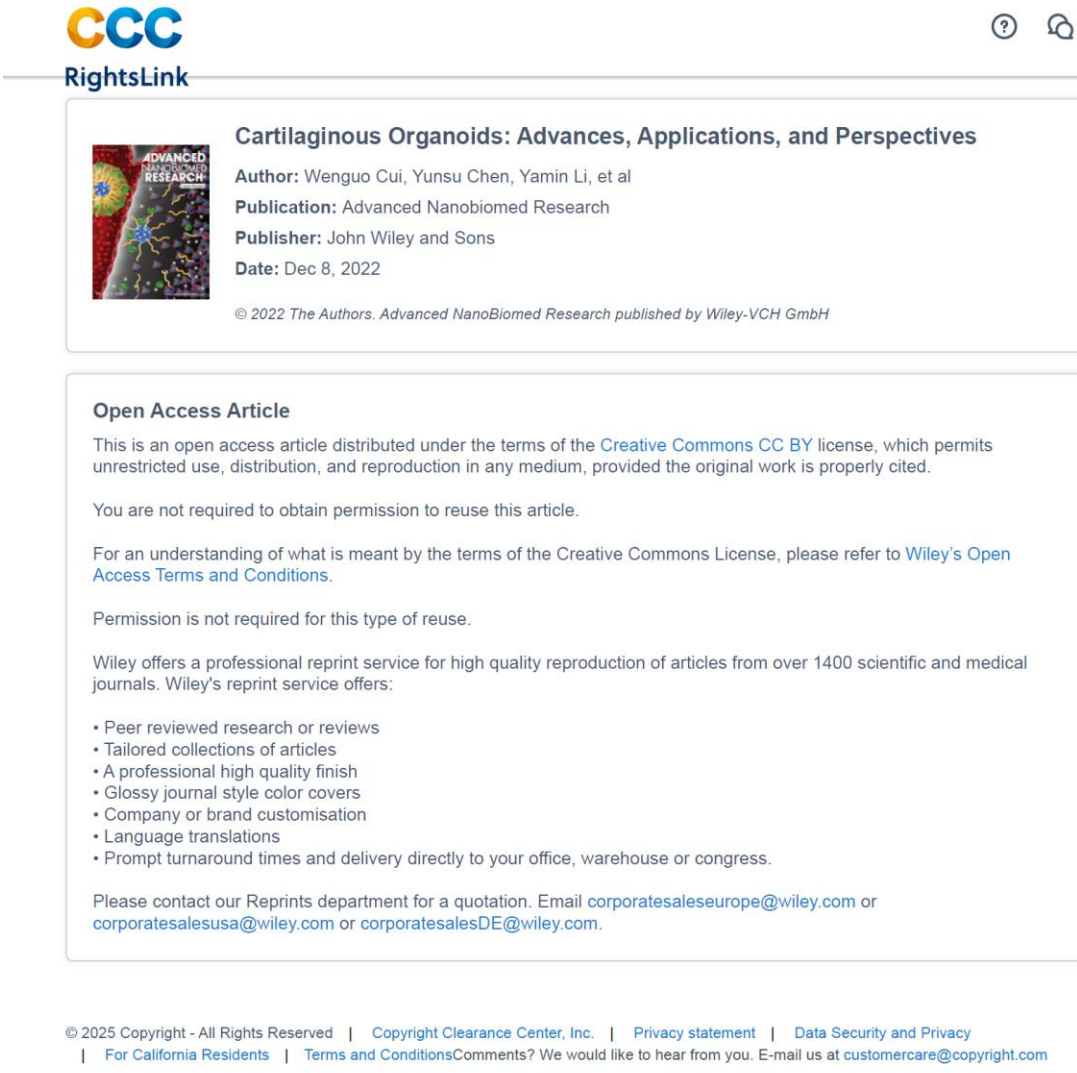

RightsLink

Cartilaginous Organoids: Advances, Applications, and Perspectives

Author: Wenguo Cui, Yunsu Chen, Yamin Li, et al

Publication: Advanced Nanobiomed Research

Publisher: John Wiley and Sons

Date: Dec 8, 2022

Open Access Article

Permission to reproduce Figure 3.4

Open Access | Feature Paper | Editor's Choice | Article

Quantitative Microstructural Analysis and X-ray Computed Tomography of Ores and Rocks—Comparison of Results

by **Oleg Popov** [1], **Irina Talovina** [2], **Holger Lieberwirth** [1,*] and **Asiia Duriagina** [2]

[1] Institute of Mineral Processing Machines, TU Bergakademie Freiberg, Lampadiusstr. 4, 09599 Freiberg, Germany

[2] Department of Historical and Dynamic Geology, Saint-Petersburg Mining University, 22 line, 2, 199106 St-Petersburg, Russia

[*] Author to whom correspondence should be addressed.

Minerals **2020**, *10*(2), 129; **https://doi.org/10.3390/min10020129**

Submission received: 9 January 2020 / Revised: 23 January 2020 / Accepted: 24 January 2020 / Published: 31 January 2020

(This article belongs to the Special Issue **Comminution in the Minerals Industry**)

Abstract

Profound knowledge of the structure and texture of rocks and ores as well as the behavior of the materials under external loads is essential to further improvements in size reduction processes, particularly in terms of liberation size. New analytical methods such as computer tomography (CT) were adopted to improve the understanding of material characteristics in rocks and ores relevant to mineral processing, particular the crushing and grinding and the modelling/simulation thereof. Results obtained on the texture and structure of identical samples of rather different rocks and ores (copper ore, granodiorite, kimberlite) are compared by CT with quantitative results from traditional optical microscopy obtained by quantitative microstructural analysis (QMA). While the two approaches show a good agreement of the results in many areas, the measurements with the two different methods also exhibit remarkable differences in other areas, which are discussed further. In conclusion, both methods have their specific advantages starting from sample preparation to the accuracy of information obtained concerning certain parameters of mode and fabric. While sample preparation is faster with CT and information on special distribution of metal minerals is more reliable, the information on mode, grain size and clustering seem to be more precise with QMA. Based on the results, it can be concluded that both methods are comparable in many areas, but in in the field of spatial distribution, they are merely complementary.

Permission to reproduce Chapter 6

CCC Marketplace

This is a License Agreement between Amanveer Singh ("User") and Copyright Clearance Center, Inc. ("CCC") on behalf of the Rightsholder identified in the order details below. The license consists of the order details, the Marketplace Permissions General Terms and Conditions below, and any Rightsholder Terms and Conditions which are included below.

All payments must be made in full to CCC in accordance with the Marketplace Permissions General Terms and Conditions below.

Order Date	02-Jul-2025	Type of Use	Republish in a thesis/dissertation
Order License ID	1626750-1	Publisher	TAYLOR & FRANCIS LTD
ISSN	1607-8438	Portion	Chapter/article

LICENSED CONTENT

Publication Title	Connective tissue research	Publication Type	e-Journal
Article Title	Assessment of articular cartilage degradation in response to an impact injury using μMRI	Start Page	146
		End Page	160
Date	01/01/1972	Issue	2
Language	English	Volume	65
Country	United Kingdom of Great Britain and Northern Ireland	URL	http://firstsearch.oclc.org
Rightsholder	Taylor & Francis Informa UK Ltd - Journals		

REQUEST DETAILS

Portion Type	Chapter/article	Rights Requested	Main product
Page Range(s)	55-66	Distribution	United States
Total Number of Pages	12	Translation	Original language of publication
Format (select all that apply)	Print, Electronic	Copies for the Disabled?	No
Who Will Republish the Content?	Author of requested content	Minor Editing Privileges?	No
Duration of Use	Current edition and up to 5 years	Incidental Promotional Use?	No
Lifetime Unit Quantity	Up to 499	Currency	USD

NEW WORK DETAILS

Title	MULTIMODAL IMAGING ASSESSMENT OF POST-TRAUMATIC OSTEOARTHRITIS PROGRESSION	Institution Name	Oakland University
		Expected Presentation Date	2025-08-30
Instructor Name	Amanveer Singh		

ADDITIONAL DETAILS

The Requesting Person / Organization to Appear on the License	Amanveer Singh

REQUESTED CONTENT DETAILS

Title, Description or Numeric Reference of the Portion(s)	Assessment of articular cartilage degradation in response to an impact injury using μMRI	Title of the Article / Chapter the Portion Is From	Assessment of articular cartilage degradation in response to an impact injury using μMRI
Editor of Portion(s)	Singh, Amanveer; Mantebea, Hannah; Badar, Farid; Batool, Syeda; Abdelmessih, Gabrielle; Sebastian, Talia; Newton, Michael; Baker, Kevin; Salem, Sarah; Xia, Yang	Author of Portion(s)	Singh, Amanveer; Mantebea, Hannah; Badar, Farid; Batool, Syeda; Abdelmessih, Gabrielle; Sebastian, Talia; Newton, Michael; Baker, Kevin; Salem, Sarah; Xia, Yang
Volume / Edition	65	Publication Date of Portion	2024-03-03
Page or Page Range of Portion	146-160		

Permission to reproduce Chapter 7

JOHN WILEY AND SONS LICENSE
TERMS AND CONDITIONS

Jul 01, 2025

This Agreement between Amanveer Singh ("You") and John Wiley and Sons ("John Wiley and Sons") consists of your license details and the terms and conditions provided by John Wiley and Sons and Copyright Clearance Center.

License Number	6060471161886
License date	Jul 01, 2025
Licensed Content Publisher	John Wiley and Sons
Licensed Content Publication	Journal of Anatomy
Licensed Content Title	Assessment of post-trauma microstructural alterations in the rabbit knee cartilage and subchondral bone
Licensed Content Author	Hannah Mantebea, Farid Badar, Syeda Batool, et al
Licensed Content Date	Jun 24, 2024
Licensed Content Volume	245
Licensed Content Issue	5
Licensed Content Pages	11

Type of use	Dissertation/Thesis
Requestor type	Author of this Wiley article
Format	Print and electronic
Portion	Full article
Will you be translating?	No
Title of new work	MULTIMODAL IMAGING ASSESSMENT OF POST-TRAUMATIC OSTEOARTHRITIS PROGRESSION
Institution name	Oakland University
Expected presentation date	Aug 2025
The Requesting Person / Organization to Appear on the License	Amanveer Singh
Requestor Location	AUBURN HILLS, MI 48326 United States
Publisher Tax ID	EU826007151
Total	0.00 USD

APPENDIX B

RESEARCH ACTIVITY APPROVAL FOR ANIMAL SUBJECTS

Yang Xia, PhD
Department of Physics
Oakland University

May 24, 2013

Dr. Yang,

In response to your memo dated May 22, 2013, concerning submission of a new proposal to NIH (National Institutes of Health) which proposes to study post-traumatic osteoarthritis using a rabbit model, your animal protocol and procedures in this proposal are exempt from Oakland University's IACUC (Institutional Animal Care and Use Committee) review for the following reasons:

- The use of animal tissues from local slaughterhouse: IACUC approval is not required if the collection of animal tissues takes place postmortem and as a by-product of a commercial enterprise. Due to the nature and source of the tissue acquisition there is no potential for disease transmission to present colony animals nor is there any occupational health and safety concerns of disease transmission to humans.
- The use of animal tissues acquired from animals euthanized as part of an unrelated experiment: The harvest of tissues from dead animals itself is not considered research under the AWAR (Animal Welfare Act Regulations) and therefore, is not a regulated activity. The animal protocols in the collaborators' institutions, from which you will be receiving animal tissues, have been approved by their respective Institutional Animal Care and Use Committees.

NIH/OPRR (Office for Protection from Research Risks) considers the use of shared tissues and slaughterhouse material to be an effective application of Reduction, Refinement, and Replacement, and it encourages this practice. PHS (Public Health Service) grant applicants using shared animal tissues or slaughterhouse specimens are advised to specify the origin of tissues when describing their proposed use in an application. If the "No" box is checked on the vertebrate animal block on the face page of the PHS application form, any reference to the use of animals in the application is likely to trigger questions about IACUC approval. To avoid delays in peer review, please be advised to explain in the PHS grant application that tissues come from a slaughterhouse or as a by-product of other IACUC-approved activities.

Once the collaborating institutions' protocol approval information is forwarded to Oakland University's IACUC it will be placed on file along with this letter of exemption.

Thank you,

Shravan K. Chintala, PhD
IACUC Chair

REFERENCES

1. Anderson, D.D., et al., *Post-traumatic osteoarthritis: improved understanding and opportunities for early intervention.* J Orthop Res, 2011. **29**(6): p. 802-9.
2. Loeser, R.F., et al., *Osteoarthritis: a disease of the joint as an organ.* Arthritis Rheum, 2012. **64**(6): p. 1697-707.
3. Goldring, M.B. and S.R. Goldring, *Osteoarthritis.* J Cell Physiol, 2007. **213**(3): p. 626-34.
4. Buckwalter, J.A., H.J. Mankin, and A.J. Grodzinsky, *Articular cartilage and osteoarthritis.* Instr Course Lect, 2005. **54**: p. 465-80.
5. Zernia, G. and D. Huster, *Collagen dynamics in articular cartilage under osmotic pressure.* NMR Biomed, 2006. **19**(8): p. 1010-9.
6. Maroudas, A., M.T. Bayliss, and M.F. Venn, *Further studies on the composition of human femoral head cartilage.* Ann Rheum Dis, 1980. **39**(5): p. 514-23.
7. Sophia Fox, A.J., A. Bedi, and S.A. Rodeo, *The basic science of articular cartilage: structure, composition, and function.* Sports Health, 2009. **1**(6): p. 461-8.
8. Buckwalter, J.A. and H.J. Mankin, *Articular cartilage: tissue design and chondrocyte-matrix interactions.* Instr Course Lect, 1998. **47**: p. 477-86.
9. Xia, Y., *Averaged and depth-dependent anisotropy of articular cartilage by microscopic imaging.* Semin Arthritis Rheum, 2008. **37**(5): p. 317-27.
10. Mankin, H.J., *The response of articular cartilage to mechanical injury.* J Bone Joint Surg Am, 1982. **64**(3): p. 460-6.
11. Peterfy, C.G., et al., *Whole-Organ Magnetic Resonance Imaging Score (WORMS) of the knee in osteoarthritis.* Osteoarthritis Cartilage, 2004. **12**(3): p. 177-90.
12. Nemec, U., et al., *MRI versus radiography of acromioclavicular joint dislocation.* AJR Am J Roentgenol, 2011. **197**(4): p. 968-73.
13. Pakin, S.K., et al., *Ultra-high-field MRI of knee joint at 7.0T: preliminary experience.* Acad Radiol, 2006. **13**(9): p. 1135-42.
14. Choi, J.A. and G.E. Gold, *MR imaging of articular cartilage physiology.* Magn Reson Imaging Clin N Am, 2011. **19**(2): p. 249-82.
15. Flandry, F. and G. Hommel, *Normal anatomy and biomechanics of the knee.* Sports Med Arthrosc Rev, 2011. **19**(2): p. 82-92.
16. Abulhasan, J.F. and M.J. Grey, *Anatomy and Physiology of Knee Stability.* Journal of Functional Morphology and Kinesiology, 2017. **2**(4): p. 34.
17. Ahmed, A.M. and D.L. Burke, *In-vitro measurement of static pressure distribution in synovial joints--Part I: Tibial surface of the knee.* J Biomech Eng, 1983. **105**(3): p. 216-25.
18. Makris, E.A., P. Hadidi, and K.A. Athanasiou, *The knee meniscus: structure-function, pathophysiology, current repair techniques, and prospects for regeneration.* Biomaterials, 2011. **32**(30): p. 7411-31.
19. Ellison, A.E. and E.E. Berg, *Embryology, anatomy, and function of the anterior cruciate ligament.* Orthop Clin North Am, 1985. **16**(1): p. 3-14.

20. Benjamin, M., E. Kaiser, and S. Milz, *Structure-function relationships in tendons: a review.* J Anat, 2008. **212**(3): p. 211-28.
21. Hughston, J.C., et al., *Classification of knee ligament instabilities. Part I. The medial compartment and cruciate ligaments.* J Bone Joint Surg Am, 1976. **58**(2): p. 159-72.
22. Chatra, P.S., *Bursae around the knee joints.* Indian J Radiol Imaging, 2012. **22**(1): p. 27-30.
23. Hügle, T. and J. Geurts, *What drives osteoarthritis?-synovial versus subchondral bone pathology.* Rheumatology (Oxford), 2017. **56**(9): p. 1461-1471.
24. Mow, V.C., et al., *Biphasic creep and stress relaxation of articular cartilage in compression? Theory and experiments.* J Biomech Eng, 1980. **102**(1): p. 73-84.
25. Maroudas, A. and M. Venn, *Chemical composition and swelling of normal and osteoarthrotic femoral head cartilage. II. Swelling.* Ann Rheum Dis, 1977. **36**(5): p. 399-406.
26. Torzilli, P.A., D.E. Rose, and D.A. Dethmers, *Equilibrium water partition in articular cartilage.* Biorheology, 1982. **19**(4): p. 519-37.
27. Huber, M., S. Trattnig, and F. Lintner, *Anatomy, biochemistry, and physiology of articular cartilage.* Invest Radiol, 2000. **35**(10): p. 573-80.
28. Eyre, D.R., *The collagens of articular cartilage.* Semin Arthritis Rheum, 1991. **21**(3 Suppl 2): p. 2-11.
29. Roughley, P.J. and J.S. Mort, *The role of aggrecan in normal and osteoarthritic cartilage.* J Exp Orthop, 2014. **1**(1): p. 8.
30. Sodhi, H. and A. Panitch, *Glycosaminoglycans in Tissue Engineering: A Review.* Biomolecules, 2020. **11**(1).
31. Hunziker, E.B., T.M. Quinn, and H.J. Häuselmann, *Quantitative structural organization of normal adult human articular cartilage.* Osteoarthritis Cartilage, 2002. **10**(7): p. 564-72.
32. Urban, J.P., *The chondrocyte: a cell under pressure.* Br J Rheumatol, 1994. **33**(10): p. 901-8.
33. Mitrovic, D., et al., *Cell density of adult human femoral condylar articular cartilage. Joints with normal and fibrillated surfaces.* Lab Invest, 1983. **49**(3): p. 309-16.
34. Fernandes, J.C., J. Martel-Pelletier, and J.P. Pelletier, *The role of cytokines in osteoarthritis pathophysiology.* Biorheology, 2002. **39**(1-2): p. 237-46.
35. Zhang, Y. and J.M. Jordan, *Epidemiology of osteoarthritis.* Clin Geriatr Med, 2010. **26**(3): p. 355-69.
36. Hunter, D.J. and D.T. Felson, *Osteoarthritis.* Bmj, 2006. **332**(7542): p. 639-42.
37. Sokolove, J. and C.M. Lepus, *Role of inflammation in the pathogenesis of osteoarthritis: latest findings and interpretations.* Ther Adv Musculoskelet Dis, 2013. **5**(2): p. 77-94.
38. McCoy, A.M., *Animal Models of Osteoarthritis: Comparisons and Key Considerations.* Vet Pathol, 2015. **52**(5): p. 803-18.
39. Bendele, A.M., *Animal models of osteoarthritis.* J Musculoskelet Neuronal Interact, 2001. **1**(4): p. 363-76.

40. Xu, Z., et al., *Biomechanical assessment of disease outcome in surgical interventions for medial meniscal posterior root tears: a finite element analysis.* BMC Musculoskelet Disord, 2022. **23**(1): p. 1093.
41. Yu, Y., et al., *Cartilaginous Organoids: Advances, Applications, and Perspectives.* Advanced NanoBiomed Research, 2023. **3**(1): p. 2200114.
42. Buckland-Wright, J.C., et al., *Accuracy and precision of joint space width measurements in standard and macroradiographs of osteoarthritic knees.* Ann Rheum Dis, 1995. **54**(11): p. 872-80.
43. Vignon, E., et al., *Measurement of radiographic joint space width in the tibiofemoral compartment of the osteoarthritic knee: comparison of standing anteroposterior and Lyon schuss views.* Arthritis Rheum, 2003. **48**(2): p. 378-84.
44. Plewes, D.B. and W. Kucharczyk, *Physics of MRI: a primer.* J Magn Reson Imaging, 2012. **35**(5): p. 1038-54.
45. Novakofski, K.D., et al., *High-Resolution Methods for Diagnosing Cartilage Damage In Vivo.* Cartilage, 2016. **7**(1): p. 39-51.
46. Haacke, E.M., et al., *Magnetic Resonance Imaging: Physical Principles and Sequence Design*. 1999: Wiley.
47. Shellock, F.G., *MR imaging of metallic implants and materials: a compilation of the literature.* AJR Am J Roentgenol, 1988. **151**(4): p. 811-4.
48. Jung, B.A. and M. Weigel, *Spin echo magnetic resonance imaging.* J Magn Reson Imaging, 2013. **37**(4): p. 805-17.
49. Conaghan, P., *Is MRI useful in osteoarthritis?* Best Pract Res Clin Rheumatol, 2006. **20**(1): p. 57-68.
50. Eckstein, F., D. Burstein, and T.M. Link, *Quantitative MRI of cartilage and bone: degenerative changes in osteoarthritis.* NMR Biomed, 2006. **19**(7): p. 822-54.
51. Burstein, D. and M.L. Gray, *Is MRI fulfilling its promise for molecular imaging of cartilage in arthritis?* Osteoarthritis Cartilage, 2006. **14**(11): p. 1087-90.
52. Alhadlaq, H.A. and Y. Xia, *The structural adaptations in compressed articular cartilage by microscopic MRI (μMRI) T2 anisotropy.* Osteoarthritis Cartilage, 2004. **12**(11): p. 887-94.
53. Kurkijärvi, J.E., et al., *Delayed gadolinium-enhanced MRI of cartilage (dGEMRIC) and T2 characteristics of human knee articular cartilage: topographical variation and relationships to mechanical properties.* Magn Reson Med, 2004. **52**(1): p. 41-6.
54. Xia, Y., *Relaxation anisotropy in cartilage by NMR microscopy (μMRI) at 14-micron resolution.* Magn Reson Med, 1998. **39**(6): p. 941-9.
55. Xia, Y., et al., *Anisotropic properties of bovine nasal cartilage.* Microsc Res Tech, 2012. **75**(3): p. 300-6.
56. Kliger, D.S. and J.W. Lewis, *Polarized Light in Optics and Spectroscopy*. 2012: Academic Press.
57. Modis, L., *Organization of the Extracellular Matrix*. 1990: Taylor & Francis.
58. Oldenbourg, R. and G. Mei, *New polarized light microscope with precision universal compensator.* J Microsc, 1995. **180**(Pt 2): p. 140-7.
59. Wolman, M., *Polarized light microscopy as a tool of diagnostic pathology.* J Histochem Cytochem, 1975. **23**(1): p. 21-50.

60. Xia, Y., et al., *Imaging the physical and morphological properties of a multi-zone young articular cartilage at microscopic resolution.* J Magn Reson Imaging, 2003. **17**(3): p. 365-74.
61. Xia, Y., et al., *Quantitative in situ correlation between microscopic MRI and polarized light microscopy studies of articular cartilage.* Osteoarthritis Cartilage, 2001. **9**(5): p. 393-406.
62. Lee, J.H. and Y. Xia, *Quantitative zonal differentiation of articular cartilage by microscopic magnetic resonance imaging, polarized light microscopy, and Fourier-transform infrared imaging.* Microsc Res Tech, 2013. **76**(6): p. 625-32.
63. Alhadlaq, H.A., et al., *Detecting structural changes in early experimental osteoarthritis of tibial cartilage by microscopic magnetic resonance imaging and polarised light microscopy.* Ann Rheum Dis, 2004. **63**(6): p. 709-17.
64. Hounsfield, G.N., *Computed medical imaging. Nobel lecture, Decemberr 8, 1979.* J Comput Assist Tomogr, 1980. **4**(5): p. 665-74.
65. Burr, D.B. and M.A. Gallant, *Bone remodelling in osteoarthritis.* Nat Rev Rheumatol, 2012. **8**(11): p. 665-73.
66. McErlain, D.D., et al., *Study of subchondral bone adaptations in a rodent surgical model of OA using in vivo micro-computed tomography.* Osteoarthritis Cartilage, 2008. **16**(4): p. 458-69.
67. Li, G., et al., *Subchondral bone in osteoarthritis: insight into risk factors and microstructural changes.* Arthritis Res Ther, 2013. **15**(6): p. 223.
68. Botter, S.M., et al., *Quantification of subchondral bone changes in a murine osteoarthritis model using micro-CT.* Biorheology, 2006. **43**(3,4): p. 379-88.
69. Potts, P.J., *Inductively coupled plasma—atomic emission spectrometry*, in *A Handbook of Silicate Rock Analysis*, P.J. Potts, Editor. 1992, Springer US: Boston, MA. p. 153-197.
70. Popov, O., et al., *Quantitative Microstructural Analysis and X-ray Computed Tomography of Ores and Rocks—Comparison of Results.* Minerals, 2020. **10**(2): p. 129.
71. Leucht, F., et al., *Development of a new biomechanically defined single impact rabbit cartilage trauma model for in vivo-studies.* J Invest Surg, 2012. **25**(4): p. 235-41.
72. Badar, F. and Y. Xia, *Image interpolation improves the zonal analysis of cartilage T2 relaxation in MRI.* Quant Imaging Med Surg, 2017. **7**(2): p. 227-237.
73. Zheng, S. and Y. Xia, *Multi-components of T2 relaxation in ex vivo cartilage and tendon.* J Magn Reson, 2009. **198**(2): p. 188-96.
74. Xia, Y., *Magic-angle effect in magnetic resonance imaging of articular cartilage: a review.* Invest Radiol, 2000. **35**(10): p. 602-21.
75. Lesperance, L.M., M.L. Gray, and D. Burstein, *Determination of fixed charge density in cartilage using nuclear magnetic resonance.* J Orthop Res, 1992. **10**(1): p. 1-13.
76. Zheng, S. and Y. Xia, *The impact of the relaxivity definition on the quantitative measurement of glycosaminoglycans in cartilage by the MRI dGEMRIC method.* Magn Reson Med, 2010. **63**(1): p. 25-32.

77. Xia, Y., *Resolution 'scaling law' in MRI of articular cartilage.* Osteoarthritis Cartilage, 2007. **15**(4): p. 363-5.
78. Pond, M.J. and G. Nuki, *Experimentally-induced osteoarthritis in the dog.* Ann Rheum Dis, 1973. **32**(4): p. 387-8.
79. Blumenkrantz, G. and S. Majumdar, *Quantitative magnetic resonance imaging of articular cartilage in osteoarthritis.* Eur Cell Mater, 2007. **13**: p. 76-86.
80. Xia, Y., *MRI of articular cartilage at microscopic resolution.* Bone Joint Res, 2013. **2**(1): p. 9-17.
81. Li, X., et al., *In vivo T(1rho) and T(2) mapping of articular cartilage in osteoarthritis of the knee using 3 T MRI.* Osteoarthritis Cartilage, 2007. **15**(7): p. 789-97.
82. Stahl, R., et al., *MRI-derived T2 relaxation times and cartilage morphometry of the tibio-femoral joint in subjects with and without osteoarthritis during a 1-year follow-up.* Osteoarthritis Cartilage, 2007. **15**(11): p. 1225-34.
83. Hannila, I., et al., *Topographical variation of T2 relaxation time in the young adult knee cartilage at 1.5 T.* Osteoarthritis Cartilage, 2009. **17**(12): p. 1570-5.
84. Batool, S., et al., *Quantitative μMRI and PLM study of rabbit humeral and femoral head cartilage at sub-10 μm resolutions.* J Orthop Res, 2020. **38**(5): p. 1052-1062.
85. Dunn, T.C., et al., *T2 relaxation time of cartilage at MR imaging: comparison with severity of knee osteoarthritis.* Radiology, 2004. **232**(2): p. 592-8.
86. Kajabi, A.W., et al., *Evaluation of articular cartilage with quantitative MRI in an equine model of post-traumatic osteoarthritis.* J Orthop Res, 2021. **39**(1): p. 63-73.
87. Terracciano, R., et al., *Quantitative high-resolution 7T MRI to assess longitudinal changes in articular cartilage after anterior cruciate ligament injury in a rabbit model of post-traumatic osteoarthritis.* Osteoarthr Cartil Open, 2022. **4**(2): p. 100259.
88. Singh, A., et al., *Assessment of articular cartilage degradation in response to an impact injury using μMRI.* Connect Tissue Res, 2024. **65**(2): p. 146-160.
89. Radin, E.L. and R.M. Rose, *Role of subchondral bone in the initiation and progression of cartilage damage.* Clin Orthop Relat Res, 1986(213): p. 34-40.
90. Kuyinu, E.L., et al., *Animal models of osteoarthritis: classification, update, and measurement of outcomes.* J Orthop Surg Res, 2016. **11**: p. 19.
91. Mantebea, H., et al., *Characteristics of distal femoral articular cartilage in 6 weeks posttraumatic osteoarthritis by a subcritical impact.* J Orthop Res, 2024. **42**(4): p. 717-728.
92. Mow, V.C., M.H. Holmes, and W.M. Lai, *Fluid transport and mechanical properties of articular cartilage: a review.* J Biomech, 1984. **17**(5): p. 377-94.
93. Kuiper, N.J. and A. Sharma, *A detailed quantitative outcome measure of glycosaminoglycans in human articular cartilage for cell therapy and tissue engineering strategies.* Osteoarthritis Cartilage, 2015. **23**(12): p. 2233-2241.
94. Buckwalter, J.A. and H.J. Mankin, *Articular cartilage: degeneration and osteoarthritis, repair, regeneration, and transplantation.* Instr Course Lect, 1998. **47**: p. 487-504.

95. Badar, F., et al., *Topographical and zonal patterns of T2 relaxation in osteoarthritic tibial cartilage by low- and high-resolution MRI.* Magn Reson Imaging, 2021. **78**: p. 98-108.
96. Xia, Y. and K. Momot, *Biophysics and Biochemistry of Cartilage by NMR and MRI*. 2016: Royal Society of Chemistry.
97. Dijkgraaf, L.C., et al., *Normal cartilage structure, biochemistry, and metabolism: a review of the literature.* J Oral Maxillofac Surg, 1995. **53**(8): p. 924-9.
98. Roughley, P.J. and E.R. Lee, *Cartilage proteoglycans: structure and potential functions.* Microsc Res Tech, 1994. **28**(5): p. 385-97.
99. Hayes, W.C., et al., *A mathematical analysis for indentation tests of articular cartilage.* J Biomech, 1972. **5**(5): p. 541-51.
100. Watson, P.J., et al., *Cartilage swelling and loss in a spontaneous model of osteoarthritis visualized by magnetic resonance imaging.* Osteoarthritis Cartilage, 1996. **4**(3): p. 197-207.
101. DiMicco, M.A., et al., *Mechanisms and kinetics of glycosaminoglycan release following in vitro cartilage injury.* Arthritis Rheum, 2004. **50**(3): p. 840-8.
102. Badar, F. and Y. Xia, *The interface region between articular cartilage and bone by μMRI and PLM at microscopic resolutions.* Microsc Res Tech, 2022. **85**(4): p. 1483-1493.
103. Korhonen, R.K., et al., *Importance of the superficial tissue layer for the indentation stiffness of articular cartilage.* Med Eng Phys, 2002. **24**(2): p. 99-108.
104. Kajabi, A.W., et al., *Multiparametric MR imaging reveals early cartilage degeneration at 2 and 8 weeks after ACL transection in a rabbit model.* J Orthop Res, 2020. **38**(9): p. 1974-1986.
105. Mantebea, H., et al., *Structural differences between immature and mature articular cartilage of rabbits by microscopic MRI and polarized light microscopy.* J Anat, 2022. **240**(6): p. 1141-1151.
106. Olmez, N. and H.R. Schumacher, Jr., *Crystal deposition and osteoarthritis.* Curr Rheumatol Rep, 1999. **1**(2): p. 107-11.
107. Ulrich-Vinther, M., et al., *Articular cartilage biology.* J Am Acad Orthop Surg, 2003. **11**(6): p. 421-30.
108. Clark, J.M., *The structure of vascular channels in the subchondral plate.* J Anat, 1990. **171**: p. 105-15.
109. Mansfield, J.C. and C.P. Winlove, *A multi-modal multiphoton investigation of microstructure in the deep zone and calcified cartilage.* J Anat, 2012. **220**(4): p. 405-16.
110. Zizak, I., et al., *Characteristics of mineral particles in the human bone/cartilage interface.* J Struct Biol, 2003. **141**(3): p. 208-17.
111. Goldring, M.B. and S.R. Goldring, *Articular cartilage and subchondral bone in the pathogenesis of osteoarthritis.* Ann N Y Acad Sci, 2010. **1192**: p. 230-7.
112. Milz, S. and R. Putz, *Quantitative morphology of the subchondral plate of the tibial plateau.* J Anat, 1994. **185 (Pt 1)**(Pt 1): p. 103-10.
113. Madry, H., C.N. van Dijk, and M. Mueller-Gerbl, *The basic science of the subchondral bone.* Knee Surg Sports Traumatol Arthrosc, 2010. **18**(4): p. 419-33.

114. Suri, S. and D.A. Walsh, *Osteochondral alterations in osteoarthritis.* Bone, 2012. **51**(2): p. 204-11.
115. Burr, D.B., *Anatomy and physiology of the mineralized tissues: role in the pathogenesis of osteoarthrosis.* Osteoarthritis Cartilage, 2004. **12 Suppl A**: p. S20-30.
116. Alhadlaq, H.A., et al., *Morphological changes in articular cartilage due to static compression: polarized light microscopy study.* Connect Tissue Res, 2007. **48**(2): p. 76-84.
117. Wang, W., et al., *Roles of the calcified cartilage layer and its tissue engineering reconstruction in osteoarthritis treatment.* Front Bioeng Biotechnol, 2022. **10**: p. 911281.
118. Goldring, S.R., *Alterations in periarticular bone and cross talk between subchondral bone and articular cartilage in osteoarthritis.* Ther Adv Musculoskelet Dis, 2012. **4**(4): p. 249-58.
119. Kaspiris, A., et al., *Sex, but not age and bone mass index positively impact on the development of osteochondral micro-defects and the accompanying cellular alterations during osteoarthritis progression.* Chronic Dis Transl Med, 2022. **8**(1): p. 41-50.
120. Keinan-Adamsky, K., H. Shinar, and G. Navon, *The effect of detachment of the articular cartilage from its calcified zone on the cartilage microstructure, assessed by 2H-spectroscopic double quantum filtered MRI.* J Orthop Res, 2005. **23**(1): p. 109-17.
121. Revell, P.A., et al., *Metabolic activity in the calcified zone of cartilage: observations on tetracycline labelled articular cartilage in human osteoarthritic hips.* Rheumatol Int, 1990. **10**(4): p. 143-7.
122. Fan, X., et al., *The deterioration of calcified cartilage integrity reflects the severity of osteoarthritis-A structural, molecular, and biochemical analysis.* Faseb j, 2022. **36**(2): p. e22142.
123. Zhang, Y., et al., *Analysis of the mineral composition of the human calcified cartilage zone.* Int J Med Sci, 2012. **9**(5): p. 353-60.
124. Batiste, D.L., et al., *Ex vivo characterization of articular cartilage and bone lesions in a rabbit ACL transection model of osteoarthritis using MRI and micro-CT.* Osteoarthritis Cartilage, 2004. **12**(12): p. 986-96.
125. Intema, F., et al., *In early OA, thinning of the subchondral plate is directly related to cartilage damage: results from a canine ACLT-meniscectomy model.* Osteoarthritis Cartilage, 2010. **18**(5): p. 691-8.
126. Meyer, E.G., et al., *Tibiofemoral contact pressures and osteochondral microtrauma during anterior cruciate ligament rupture due to excessive compressive loading and internal torque of the human knee.* Am J Sports Med, 2008. **36**(10): p. 1966-77.
127. Bettica, P., et al., *Evidence for increased bone resorption in patients with progressive knee osteoarthritis: longitudinal results from the Chingford study.* Arthritis Rheum, 2002. **46**(12): p. 3178-84.
128. Singh, A., et al., *Assessment of post-trauma microstructural alterations in the rabbit knee cartilage and subchondral bone.* J Anat, 2024. **245**(5): p. 740-750.